Journal of Catalysis 313 (2014) 55–69

Contents lists available at ScienceDirect

Journal of Catalysis

journal homepage: www.elsevier.com/locate/jcat

Catalytic consequences of the identity and coverages of reactive intermediates during methanol partial oxidation on Pt clusters

Weifeng Tu [a,b], Ya-Huei (Cathy) Chin [a,*]

[a] Department of Chemical Engineering and Applied Chemistry, University of Toronto, Toronto, Canada
[b] College of Power Engineering, Chongqing University, Chongqing 40030, China

ARTICLE INFO

Article history:
Received 6 August 2013
Revised 2 December 2013
Accepted 29 January 2014

Keywords:
Partial oxidation
Pt cluster
Methanol
Oxygen chemical potential
Methyl formate
Formaldehyde
Oxidative dehydrogenation
Chemisorbed oxygen
Cluster size effect
Methanol oxidation

ABSTRACT

Rate measurements, carried out after elimination of transport corruptions, show that CH_3OH partial oxidation on Pt clusters proceeds via three distinctly different kinetic regimes defined by the operating oxidant-to-reductant (O_2-to-CH_3OH) ratio. These kinetic regimes, each with unique rate dependencies for HCHO, $HCOOCH_3$, and CO_2 formation, arise from a dynamic shift in the identity and coverages of reactive intermediates on Pt cluster surfaces from saturated with chemisorbed oxygen, to uncovered, and then to partially covered with methanol derived species as the oxygen chemical potential at cluster surfaces decreases with decreasing O_2-to-CH_3OH ratio. HCHO formation rates first remain insensitive to O_2 on Pt cluster surfaces saturated with chemisorbed oxygen (O^*), then increase proportionally with O_2 as cluster surfaces depleted of oxygen and as unoccupied Pt sites become the most abundant surface intermediates, and eventually increase more than linearly with O_2 on Pt surfaces predominantly covered with CH_3OH derived intermediates. The transition in rate dependence on O_2 is accompanied by a concomitant transition on CH_3OH dependence: HCHO formation rates are linearly proportional to, then independent of, and eventually inhibited by CH_3OH as the O_2-to-CH_3OH ratio decreases. Similar transition in reaction orders is also found for $HCOOCH_3$ and CO_2 formation. The first-order rate coefficient for CH_3OH oxidation is a single-valued function of the operating O_2-to-CH_3OH ratio, because the ratio determines the oxygen chemical potential at Pt cluster surfaces via the kinetic coupling of O_2 and CH_3OH activation steps and, in turn, the identity and coverage of reactive intermediates, the nature and availability of active sites, and the identity of kinetically-relevant steps.

1. Introduction

Selective catalytic oxidation of alcohol to aldehyde and ketone is an important route for synthesizing carbonyl compounds useful as chemical building blocks. Oxidation of methanol, the simplest alcohol, may occur over metal [1–8], metal oxide [9–13], or mixed oxide [14–16] catalysts and form diverse products depending on the operating temperature and oxygen-to-methanol ratios. CH_3OH–O_2 reactions form CO_x, HCHO, $HCOOCH_3$, CH_3OCH_3, and $CH_3OCH_2OCH_3$ on metal oxide (VO_x [9–11], RuO_2 [12]) or mixed oxide (SnO_2–MoO_3 [14]) structures at O_2-to-CH_3OH ratios above the stoichiometry required for HCHO formation ($O_2/CH_3OH > 0.5$) at moderate temperatures (373–450 K). At higher temperatures (423–650 K), the reaction forms similar products (CO_x, HCHO, $HCOOCH_3$, and CH_3OCH_3) except $CH_3OCH_2OCH_3$ on metal oxide and mixed oxides (V_2O_5 [9], MoO_3 [13], SnO_2–MoO_3 [14], $Fe_2(MoO_4)_3$ [15], and Fe_2O_3–MoO_3 [16]) over a wide range of O_2-to-CH_3OH ratios (0.64–4.8). CH_3OH–O_2 reactions on Group VIII and Group IB metals evolve HCHO, $HCOOCH_3$, and CO_2 at lower temperatures (313–400 K) (Pd [1], Pt [2,3], and Au [4]), and HCHO and CO_2 above 550 K (Ag [5] and Pt [2]). As the O_2-to-CH_3OH ratio decreases to less than 0.5, H_2 (and CO_x) begin to form on supported Pt (428–493 K) [6], Pd (428–493 K) [6], and Au (483–583 K) [7] catalysts.

CH_3OH–O_2 reactions on transition metal oxides (RuO_2 [12], Fe_2O_3–MoO_3 [16]) involve a Mars-van Krevelen-type redox cycle that shuffles lattice oxygen atoms ($O_{lattice}$) during CH_3OH turnovers [17]. Metal and lattice oxygen site pairs first cleave the O–H bond in CH_3OH, which forms adsorbed methoxy (CH_3O^*) and $O_{lattice}H^*$ intermediates, and the sequential C–H bond dissociation of CH_3O^* by another lattice oxygen forms $O_{lattice}H^*$ and $HCHO^*$ intermediates [18]. Sequential desorption of $HCHO^*$ and recombinative desorption of $O_{lattice}H^*$ intermediates lead to HCHO and H_2O, respectively, leaving behind a lattice oxygen vacancy on oxide surfaces [12,16,18], on which O_2 dissociates to complete a catalytic turn-

---

* Corresponding author. Fax: +416 978 8605.
E-mail address: cathy.chin@utoronto.ca (Ya-Huei (Cathy) Chin).

http://dx.doi.org/10.1016/j.jcat.2014.01.018
0021-9517/© 2014 Elsevier Inc. All rights reserved.

over. The H abstraction and O* addition on HCHO* lead to formate species (HCO_2^*) that may undergo secondary reactions with CH_3OH derived species to produce $HCOOCH_3$ [1,19,20] and, in parallel to these steps, C–H bond cleavage on formate species (HCO_2^*) and their sequential desorption evolve CO_x [19,20]. On metal surfaces, CH_3OH–O_2 reactions also begin with O–H scission followed by C–H activation, but these steps occur on metal atom sites, as confirmed from density functional theory calculations on uncovered Pt(1 1 1) [21] and Ag(1 1 1) [22] surfaces. Temperature-programmed desorption carried out after CH_3OD decomposition on oxygen covered Pt(1 1 1) surfaces (0.25 ML, 115–140 K) provides the evidence that O–H bond cleavage remains as the initial step but with O* involvement [23]. Decomposition of methoxide, an intermediate from CH_3OH activation, on bare metal surfaces {Pt(1 1 1) [21] and Ni(1 1 0) [24]}, forms CO and H_2, but in the presence of surface oxygen {Ni(1 1 0) [24], Cu(1 1 0) [25]}, oxygen insertion and H abstraction become the predominant route to evolve formate species, which decompose sequentially to CO_2 and H_2.

The catalytic steps, their kinetic relevance, and the identity and coverages of surface intermediates are known to dictate kinetic dependencies and carbon selectivities toward the primary (HCHO) and secondary (CO_2, $HCOOCH_3$, $CH_3OCH_2OCH_3$) products. The specific catalytic events and their rates are known to also vary with the identity and chemical state of metal and oxygen (e.g., lattice oxygen, chemisorbed oxygen), the latter depends largely on the operating temperature [2,26] and pressures of reactants and products [5,12]. The intricate connection among the gas-phase composition, identity and types of surface sites, and relative rates of CH_3OH and O_2 activation leads to complex kinetic behavior with wide ranging and often contradictory kinetic dependencies. As a result, the identity of the kinetically-relevant step ranges from C–H bond activation of CH_3OH derived intermediates (CH_3O^*) [5,12,16], desorption of the HCHO* intermediates [27], to activation of O_2 [4,5].

Lattice oxygen [12], chemisorbed diatomic [28–30], or monoatomic oxygen [23] atoms have been proposed to involve as active species in CH_3OH–O_2 reactions. Molybdenum oxide structures saturated with oxygen were found to be effective toward CH_3OH activation but their reactivity decreased with depletion of lattice oxygen from their reactions with CH_3OH [31]. The terminal lattice oxygen atom ($O_{lattice}$) on VO_x [9], MoO_x [32], and mixed oxides (Fe_2O_3–MoO_3 [16]), together with a vicinal metal ion, forms a site pair that assists the initial O–H bond dissociation in CH_3OH to form CH_3O^*, followed by sequential C–H cleavage of the CH_3O^* by another vicinal lattice oxygen [18]. Chemisorbed oxygen (O*) on Au [4,33], Ag [34], Pt [28], and Pd [35] may also promote CH_3OH dissociation. Infrared reflection absorption spectroscopy (IRAS) and temperature desorption studies on CH_3OH reactions with pre-adsorbed molecular oxygen on Pt(1 1 1) (0.34 ML O_2^* at 35–100 K [29] and 0.5 ML O_2^* at 100–550 K [28,36]) and pre-adsorbed atomic oxygen (0.25 ML O*) on Pd(1 1 1) [35] or Pt(1 1 1) [28,36] surfaces at 100–550 K suggest mechanistic involvements of both types of oxygen species toward CH_3OH activation. Methanol adsorbs weakly on bare metal surfaces (Au(1 1 1) [33] or Au(1 1 0) [37]) but reacts readily with pre-adsorbed atomic oxygen on such surfaces (Au(1 1 1) [33], Au(1 1 0) [37], Ag (1 1 0) [34], and Cu(1 1 0) [38]) to form methoxy and hydroxyl species, in a mechanistic step similar to those proposed on lattice oxygen-metal pairs on metal oxide structures [9,12]. O* may also assist with the sequential H abstraction of CH_3O^* to evolve HCHO [25] or alternatively, insert into the CH_3O^* and, upon C–H cleavage, to form H_2COO^* and H* [38]. The catalytic function of oxygen has been recognized, but the mechanistic consequences of their coverages and binding strength have yet to be established.

Here, we report diverse rate dependencies and their transition during CH_3OH–O_2 reactions on Pt clusters, probe the nature of catalytic sites, and provide a mechanistic explanation to these kinetic phenomena. We provide the evidence that these kinetic phenomena are of true chemical origin, based on rate data obtained strictly in the kinetically controlled regime, after extensive intra- and inter-pellet dilutions to remove temperature and concentration gradients within the catalyst pellets and reactor bed. Kinetics of CH_3OH oxidation are described by three distinctly different regimes, each with a unique rate equation for CH_3OH conversion to HCHO, the primary product, and exhibits different carbon selectivity dependencies toward $HCOOCH_3$ and CO_2. These regimes are caused by a dynamic transition of the coverages and identity of reactive intermediates on Pt cluster surfaces from saturated with O*, uncovered, to covered with CH_3OH derived species as the oxygen chemical potential at cluster surfaces decreases. We interpret each of the regimes with a closed sequence of elementary steps and probe the change in their kinetic relevance. We vary the mean Pt cluster diameter to probe the effects of surface Pt coordination and binding strengths on rates and selectivities. The first-order rate coefficient is a single-valued function of the O_2/CH_3OH ratio, because O_2/CH_3OH ratio prescribes the identity and coverages of reactive intermediates that dictate, in turn, the specific catalytic events and their rates. These dynamic transitions of rate dependencies in response to changing surface coverages and chemical potentials are also found during alkane oxidation (CH_4 [39,40], C_2H_6 [41]); they reflect how thermodynamic properties at catalytic sites dictate the relative abundance of surface intermediates and the identity of kinetically-relevant step during oxidation catalysis.

2. Catalyst preparation and experimental methods

2.1. Synthesis and characterizations of supported Pt clusters and preparation of catalyst samples with varying inter- and intra-particle dilution ratios

Silica (Grace, Davisil Chromatographic Silica, 330 $m^2\ g^{-1}$ surface area, 1.25 $cm^3\ g^{-1}$ pore volume, 0–75 μm particle size) was treated under ambient air by increasing the temperature at 0.033 $K\ s^{-1}$ to 673 K followed by holding for 3 h at 673 K before cooling to 393 K. The sample was kept at 393 K until the impregnation step to prevent readsorption of water. Pt clusters were dispersed on the treated silica at a loading of 1.0 wt% by incipient wetness impregnation with an aqueous solution of tetraammineplatinum(II) nitrate ($Pt(NH_3)_4(NO_3)_2$, Sigma Aldrich, 99.995% trace metals basis), prepared from dissolving the precursor in doubly deionized water. The impregnated sample was treated at 353 K for 24 h under ambient air and then in flowing dry air (Linde, 99.99%, 0.3 $cm^3\ g^{-1}\ s^{-1}$) by increasing the temperature at 0.05 $K\ s^{-1}$ to 673 K, holding isothermally at 673 K for 5 h. A portion of the catalysts was subsequently treated at 773 K for 5 h under flowing dry air (Linde, 99.99%, 0.3 $cm^3\ g^{-1}\ s^{-1}$, 0.05 $K\ s^{-1}$ ramp) to attain larger Pt clusters. These samples were cooled to ambient temperature and then treated in 5% H_2/He (Linde certified standard, 5.22%, 0.3 $cm^3\ g^{-1}\ s^{-1}$) by heating to 673 K at 0.033 $K\ s^{-1}$, holding isothermally at 673 K for 1 h, and then cooling to ambient temperature. The samples were introduced to 1% O_2/He (0.3 $cm^3\ g^{-1}\ s^{-1}$) for 6 h before exposure to ambient conditions.

The average Pt cluster diameter was measured from volumetric uptakes of H_2, irreversibly chemisorbed on Pt clusters, at 298 K. The catalyst samples were first treated in flowing H_2 (Linde, 99.99%, 0.2 $cm^3\ g^{-1}\ s^{-1}$) by heating from ambient temperature to 673 K at 0.083 $K\ s^{-1}$ and holding for 1 h before exposure to dynamic vacuum at 673 K for 1 h and then cooling under dynamic vacuum to 298 K for H_2 chemisorption measurements. H_2 uptakes were measured at 298 K between 0 and 13 kPa H_2; two isotherms were measured consecutively, and between these measurements, the sample was evacuated under dynamic vacuum for 0.5 h. The fractions of exposed Pt atoms were determined from the difference between the extrapolated values from the two isotherms to zero H_2 pressure and by assuming a H-to-surface Pt adsorption stoichiometry (H/Pt_s; subscript s denotes surface Pt atom) of unity. The average cluster diameters were estimated from these dispersion values by assuming hemispherical clusters with density similar to bulk Pt metal (21.45 g cm^{-3}) [42].

Catalyst samples (1.0 wt% Pt/SiO_2) were diluted with SiO_2 (Grace, Davisil Chromatographic Silica, 330 m^2 g^{-1} surface area, 1.25 cm^3 g^{-1} pore volume, 0–75 μm particle size) to form well-mixed physical mixtures at different SiO_2-to-catalyst mass ratios between 100 and 400. The physical mixtures were pressed into pellets before sieving to retain 125–180 μm agglomerates. These agglomerates were physically mixed with SiO_2 (Grace, Davisil Chromatographic Silica, 330 m^2 g^{-1} surface area, 1.25 cm^3 g^{-1} pore volume, 125–180 μm particle size) to form the packed catalyst bed with an overall SiO_2-to-catalyst mass ratio between 2000 and 5700.

2.2. Catalytic rate and selectivity measurements

The catalyst bed (containing 0.025–0.15 mg of 1.0 wt% Pt/SiO_2) was heated in flowing H_2 (Linde, 99.99%, 0.2–1.3 × 10^4 cm^3 g_{cat}^{-1} s^{-1}) to 673 K at 0.083 K s^{-1} and holding for 1 h, and then cooled to reaction temperature in flowing He (Linde, 99.999%, 0.2–1.3 × 10^4 cm^3 g_{cat}^{-1} s^{-1}) before rate measurements. CH_3OH turnover rates were measured on a packed-bed of catalyst particles (inter- and intra-particle SiO_2-to-catalyst mass ratio of 5700 and 100–400, respectively) at 310–910 K, held in a tubular micro-catalytic plug flow reactor (8.1 mm reactor ID) equipped with an axial concentric K-type thermocouple. Reactant mixtures were prepared from either 5% O_2/He (Linde certified standard, 5.03%) or pure O_2 (Linde, 99.99%), CH_3OH (Sigma Aldrich, anhydrous, 99.8%), and He (Linde, 99.999%). Gas flow rates of 5% O_2/He, pure O_2, and He were independently metered using electronic mass flow controllers to achieve a space velocity between 4.2×10^7 cm^3 $(g_{cat}\,h)^{-1}$ and 2.5×10^8 cm^3 $(g_{cat}\,h)^{-1}$. Methanol was introduced using a gas tight syringe (Hamilton, 5 cm^3) mounted on a syringe infusion pump (KD Scientific, LEGATO 100) at constant infusion rates into a heated zone maintained at 338 K, in which it was evaporated and mixed with the gas feed stream containing O_2 and He.

Turnover rates for HCHO–O_2 and $HCOOCH_3$–O_2 reactions were also measured on the catalyst samples at 310–910 K in the tubular micro-catalytic plug flow reactor. Gaseous formaldehyde (0–0.13 kPa) was prepared from decomposition of paraformaldehyde (Sigma Aldrich, 95%) into a flowing purge stream of He (Linde, 99.999%, 0–0.67 cm^3 s^{-1}) in a glass vaporizer maintained at 313 K. $HCOOCH_3$ vapor (0–0.92 kPa) in He was prepared from evaporating liquid $HCOOCH_3$ (Sigma Aldrich, anhydrous, 99%) contained in a glass vaporizer into a stream of flowing He (Linde, 99.999%, 0–0.083 cm^3 s^{-1}) at 273 K. All transfer gas lines were heated to 373 K to prevent condensation of reactants and products and polymerization of formaldehyde.

The chemical compositions of the reactant and product streams were quantified using a micro-GC (Varian CP-4900) equipped with HP-PLOT U and Mol Sieve 5A columns connected to thermal conductivity detectors. The identity of chemical species and their amounts detected by the micro-GC were confirmed using an online gas chromatograph (Agilent 7890A) with mass spectrometer (Agilent 5975C) (GC–MS) equipped with capillary columns, Agilent HP-5MS (190091S-433, 30 m, 0.25 mm ID, 0.25 μm film), connected to a thermal conductivity detector and a flame ionization detector in series and HP-5 (19091 J-413, 30 m, 0.32 mm ID, 0.25 μm film) connected to a mass selective detector. The concentration of CO in the product stream was quantified using a gas chromatograph (SRI 8610C) equipped with packed columns (Mol Sieve 13X and Hayesep D) connected to (i) a thermal conductivity detector and (ii) a methanator followed by a flame ionization detector, respectively. The concentration of H_2 in the product stream was quantified using a gas chromatograph (SRI 8610C) equipped with packed columns (Mol Sieve 13X and Hayesep D) connected to a helium ionization detector (HID).

3. Results and discussion

3.1. Assessing the intrinsic catalytic rates for CH_3OH-O_2 reactions on Pt clusters: rigorous removal of rate contributions from SiO_2 support, gas-phase reaction, and concentration and temperature gradients

Fig. 1a shows CH_3OH conversion during CH_3OH–O_2 reactions on 1.0 wt% Pt/SiO_2 catalyst (3.0 nm mean Pt cluster diameter, 0.05 mg 1.0 wt% Pt/SiO_2 and 0.285 g SiO_2), on SiO_2 (support, 0.285 g), and in the gas phase (without catalyst and support) as a function of reaction temperature, compared at the same reactant flow rate and compositions (1.0 kPa CH_3OH, 1.5 kPa O_2, 1.75 cm^3 s^{-1}, 310–910 K). Fig. 1b and 1c show selectivities of carbon-containing products as a function of temperature during CH_3OH–O_2 reactions (1.0 kPa CH_3OH, 1.5 kPa O_2, 1.75 cm^3 s^{-1}, 310–910 K) on the 1.0 wt% Pt/SiO_2 catalyst (0.05 mg 1.0 wt% Pt/SiO_2 and 0.285 g SiO_2) and on bare SiO_2 (0.285 g) samples, respectively. Gas-phase CH_3OH–O_2 reactions became detectable above 650 K (Fig. 1a) and led to CO, CO_2, HCHO, and H_2O (3.8% CH_3OH conversion; selectivities of carbon-containing products to CO, CO_2, and HCHO are 1.3%, 8.9%, and 89.8%, respectively, at 720 K, not shown here). CH_3OH conversions were detectable on bare SiO_2, the material used for dispersing Pt clusters, at lower temperatures (>450 K, Fig. 1a) and produced CO, CO_2, HCHO, $HCOOCH_3$, and H_2O (5.3% CH_3OH conversion; selectivities of carbon-containing products to CO, CO_2, HCHO, and $HCOOCH_3$ are 1.9%, 17.0%, 79.1%, and 2.0%, respectively, at 493 K, Fig. 1c). Acetalization of CH_3OH with HCHO, a product, on SiO_2 produced $HCOOCH_3$ at these temperatures (450–650 K), as also reported previously on oxides {SiO_2 [43], Al_2O_3 [12], SnO_2 [14], TiO_2 [43], and ZrO_2 [43]}. The predominant carbonaceous product was HCHO below 650 K (76.7% selectivity at 537 K) but as the temperature increased, sequential oxidation of HCHO and $HCOOCH_3$ became much faster relative to the initial catalytic CH_3OH turnover and formed CO and CO_2 as the dominant carbonaceous products (Fig. 1c). At the lower temperature range (350–390 K, Fig. 1a), CH_3OH conversion rates on 1.0 wt% Pt/SiO_2 catalyst (3.0 nm mean Pt cluster diameter) were at least two orders of magnitude higher than the combined rates on SiO_2 and in the gas phase $\{r_{CH_3OH,pt}\left(r_{CH_3OH,SiO_2} + r_{CH_3OH,\text{gas phase}}\right)^{-1} = 101.2$ at 373 K, Fig. 1a} and the reaction formed HCHO, CO_2, H_2O, and $HCOOCH_3$. As the temperature increased, the dominant carbonaceous product varied from $HCOOCH_3$ to HCHO and then to CO_2 (Fig. 1b). CO was not detected in the effluent stream at all temperatures (<5 ppmv detection limit, 310–600 K, O_2/CH_3OH = 1.5) on 1.0 wt% Pt/SiO_2 (Fig. 1b), because of much faster rates for CO than CH_3OH oxidation. The temperatures required for 50% CH_3OH conversion were 472 K, 627 K, and 850 K on Pt/SiO_2, SiO_2, and in the gas phase, respectively. At low temperatures (e.g., 373 K), HCHO and $HCOOCH_3$ did not react with O_2 on SiO_2 and in the gas phase at detectable extents. Their conversions were found to be less than 0.05% in HCHO–O_2 (0.13 kPa HCHO and 0.5–16 kPa O_2, 1.75 cm^3 s^{-1}) and $HCOOCH_3$–O_2 (0.60 kPa $HCOOCH_3$ and 0.1–40 kPa O_2, 1.75 cm^3 s^{-1}) reactions. These results, taken together, confirm that primary and secondary reactions reported herein-and-after reflect catalytic turnovers of CH_3OH on Pt clusters with negligible contributions

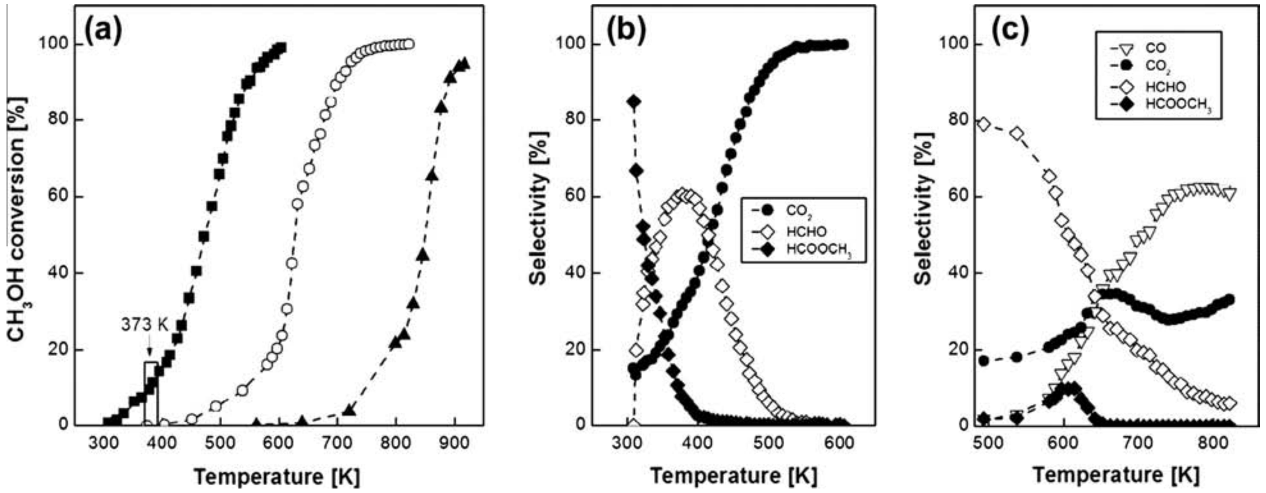

Fig. 1. (1a) CH_3OH conversion as a function of temperature during $CH_3OH–O_2$ reactions on 1.0 wt% Pt/SiO_2 (0.05 mg 1.0 wt% Pt/SiO_2 and 0.285 g SiO_2, 3.0 nm mean Pt cluster diameter) (■), on bare SiO_2 (0.285 g) (○), and in the gas phase (▲). (1b) Selectivity of carbon-containing products as a function of temperature during $CH_3OH–O_2$ reactions on 1.0 wt% Pt/SiO_2 (0.05 mg 1.0 wt% Pt/SiO_2 and 0.285 g SiO_2, 3.0 nm mean Pt cluster diameter). (1c) Selectivity of carbon-containing products as a function of temperature during $CH_3OH–O_2$ reactions on bare SiO_2 (0.285 g). (1.0 kPa of CH_3OH, 1.5 kPa of O_2, balance He; 7.7×10^{-7} (mol CH_3OH) s^{-1}).

from SiO_2 supports and the gas phase (estimated to be <1% at 373 K).

The partial and total oxidation of methanol {Eqs. (1a) and (1b)} and the sequential reactions of HCHO with CH_3OH and O_2 {Eq. (1c)} and with O_2 {Eq. (1d)} proceed with the respective standard heat of reaction (evaluated at 298 K):

$$CH_3OH + 0.5O_2 \rightarrow HCHO + H_2O \quad \Delta H^{\circ}_{298} = -155.8\ \text{kJ}\ (\text{mol}\ CH_3\ OH)^{-1} \tag{1a}$$

$$CH_3OH + 1.5O_2 \rightarrow CO_2 + 2H_2O \quad \Delta H^{\circ}_{298} = -726.5\ \text{kJ}(\text{mol}\ CH_3\ OH)^{-1} \tag{1b}$$

$$CH_3OH + HCHO + 0.5O_2 \rightarrow HCOOCH_3 + H_2O \quad \Delta H^{\circ}_{298} = -304.5\ \text{kJ}\ (\text{mol}\ CH_3\ OH)^{-1} \tag{1c}$$

$$HCHO + O_2 \rightarrow CO_2 + H_2O \quad \Delta H^{\circ}_{298} = -570.7\ \text{kJ}\ (\text{mol HCHO})^{-1} \tag{1d}$$

These exothermic reactions (−155.8 to −726.5 kJ mol^{-1}) may increase the local temperature at catalytic sites and cause significant concentration and temperature gradients within individual catalyst pellets and across the reactor bed. These gradients are ubiquitously present in oxidation reactions, because of their exothermic nature and high rates, and often corrupt rate data and their mechanistic interpretation. Here, transport corruptions were diagnosed and then rigorously removed by extensive dilutions at the intra- and inter-pellet scales with inert solids. Dilutions decrease the rate of heat release per unit volume (heat load) and, as the diluent-to-catalyst ratio increases and the heat load concomitantly decreases to the extent that does not bring forth detectable kinetic consequences, the measured rates and selectivities reflect intrinsic values evaluated at the pressures and temperature of the contacting gas phase.

Table 1 provides the maximum amount of heat released per unit catalyst bed volume from this study together with values from $CH_4–O_2$ [40], $C_2H_6–O_2$ [41], and $CH_3OCH_3–O_2$ [44] reactions in reactors with comparable dimensions (8.1 mm reactor ID, 100–250 pellet diameters). The heat release rate per unit catalyst bed volume for $CH_3OH–O_2$ reactions (<0.04 W cm^{-3}, 0.51 kPa CH_3OH, 0–6 kPa O_2, 383 K) reported herein is comparable to those of other oxidation reaction systems (<0.66 W cm^{-3}, Table 1), measured in similar reactor configurations and previously tested and confirmed to be free of transport influences. Fig. 2 shows the HCHO, CO_2, and $HCOOCH_3$ formation rates (per exposed Pt atom) measured at different O_2 pressures (0–6 kPa O_2) while keeping the CH_3OH pressure constant (0.51 kPa CH_3OH) at 383 K on catalyst pellets diluted to different extents (intra-particle SiO_2-to-Pt/SiO_2 weight ratio of 100–400). The turnover rates (per exposed Pt atom) for HCHO, CO_2, and $HCOOCH_3$ formation and the selectivity values remained identical within the experimental accuracy (estimated er-

Table 1
Summary of intra-particle and bed dilution ratios and the reactor heat loads used for assessing the intrinsic kinetics of oxidation reactions.

Reaction	Reaction temperature (K)	Total number of active sites (10^{-9} mol)	Space velocity (10^7 cm^3 $(g_{cat}\ h)^{-1}$)	Intra-particle SiO_2-to-catalyst mass ratio	Inter-particle SiO_2-to-catalyst mass ratio	Heat of reaction (kJ (mol of reductant)$^{-1}$)	Reactor diameter (mm)	Reactor heat load (W cm^{-3})
$CH_3OCH_3–O_2$[a]	473	66.70	0.12	50:1	50:1	−1460.4	8.0	0.66
$CH_4–O_2$[b]	873	0.20	5.00	200:1	2000:1	−804.3	8.1	0.35
$C_2H_6–O_2$[c]	773	n.a.	6.00	300:1	7000:1	−1428.5	8.1	0.01
$CH_3OH–O_2$	383	0.85	12.60	200:1	5700:1	−726.5	8.1	0.04

[a] Ref. [44].
[b] Ref. [40].
[c] Ref. [41]; n.a.: unavailable.

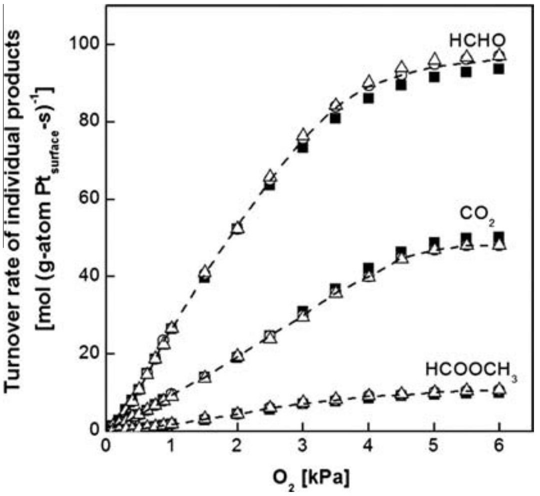

Fig. 2. Effects of intra-particle dilution ratio (SiO_2-to-catalyst mass ratio) of 100 (■), 300 (○), and 400 (Δ) on the turnover rates for HCHO, CO_2, and $HCOOCH_3$ formation (per exposed Pt atom) during CH_3OH–O_2 reactions (0.51 kPa CH_3OH, 0.0–6.0 kPa O_2) on 1.0 wt% Pt/SiO_2 (3.0 nm mean Pt cluster diameter, 383 K, 1.26×10^8 cm^3 $(g_{cat}\ h)^{-1}$, 125–180 μm pellet diameters, inter-particle dilution ratio (SiO_2-to-catalyst mass ratio) of 5700).

rors of <2%) among the samples despite the different intra-pellet dilution ratios (Fig. 2), because the overall CH_3OH conversion rates and each of the individual rates for the primary and secondary reactions were strictly proportional to the number of active site contained within the catalyst bed. These results provide the unequivocal evidence that rate and selectivity data were unaffected by temperature and concentration gradients. These findings, taken together with negligible rate contributions from SiO_2 support and homogeneous reactions of reactants and products (Fig. 1), led us to conclude that rate and selectivity data presented herein-and-after are of true chemical origin and reflect intrinsic catalytic events at Pt sites.

3.2. Primary and secondary products of methanol partial oxidation on Pt clusters

Fig. 3 shows carbon selectivities for CH_3OH–O_2 reactions as a function of CH_3OH conversion, which was varied by changing the residence time, for three O_2-to-CH_3OH feed ratios of 0.25, 1.5, and 16 on Pt clusters (1.0 wt% Pt/SiO_2, 3.0 nm mean Pt cluster diameter) at 373 K. O_2-to-CH_3OH feed ratios affect the carbon selectivity trends through their influences on the relative rates and reaction orders for the primary and secondary reactions leading to HCHO, $HCOOCH_3$, and CO_2 products. CO and H_2 were not formed (detection limits: 5 ppmv for CO and 1 ppmv for H_2) during CH_3OH oxidation on Pt clusters at 373 under all conditions tested here, covering the range of 0.01–45 O_2/CH_3OH ratios (0.08–5 kPa CH_3OH and 0.1–70 kPa O_2). At low O_2-to-CH_3OH ratios (e.g., 0.25), carbon selectivities were insensitive to CH_3OH conversion (Fig. 3a). Their values began to vary with CH_3OH conversion at higher O_2-to-CH_3OH ratios (O_2/CH_3OH = 1.5 and 16 in Fig. 3b and c, respectively): the carbon selectivities to HCHO decreased and those for $HCOOCH_3$ and CO_2 concomitantly increased as CH_3OH conversion and residence time increased. Extrapolation of carbon selectivities to zero conversion removes the rate contribution from secondary reactions and gives the selectivity values from primary CH_3OH reactions. These data indicate that at low O_2-to-CH_3OH ratios (e.g., 0.25), all products are formed directly from CH_3OH (or CH_3OH derived surface intermediates), but as the O_2-to-CH_3OH ratio increases to above 0.5, the sequential oxidation of HCHO becomes important relative to those of primary reactions, apparently because chemisorbed oxygen atoms prevalent on Pt cluster surfaces at these higher O_2-to-CH_3OH ratios are more effective for HCHO oxidation, as described in Sections 3.4 and 3.5.

The distinct variation in selectivity trends and rate dependencies (to be discussed in Section 3.3) with O_2-to-CH_3OH ratios led us to categorize the rate data according to the operating O_2/CH_3OH ratios of 0.01–0.5, 0.5–10, and 10–45 and denote these categories herein and after as Kinetic Regimes 1, 2, and 3, respectively. Next, the direct and indirect routes for HCHO, $HCOOCH_3$, and CO_2 formation from CH_3OH–O_2 mixtures and the interconversion between these products in the various pathways labeled in Scheme 1 are analyzed for each regime. HCHO–O_2 or $HCOOCH_3$–O_2 reactions were carried out in addition to CH_3OH–O_2 reactions to probe the relative rates of the primary and secondary reactions. The pseudo-first-order rate constants ($k_{P,i(n)}$) for the individual pathways in Scheme 1 are defined by the general expression of:

$$k_{P,i(n)} = \frac{r_{P,i(n)}}{[P]} \tag{2}$$

$P = CH_3OH, HCHO, or\ HCOOCH_3;\ i = \text{Kinetic Regime } 1, 2, \text{ or } 3$

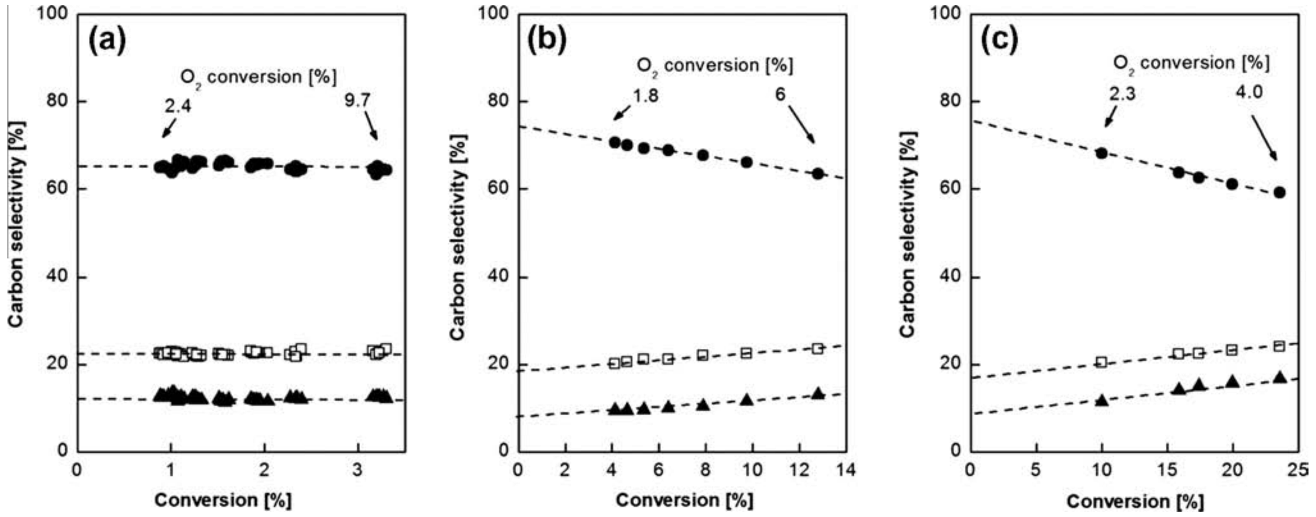

Fig. 3. Carbon selectivities toward HCHO (●), CO_2 (□), and $HCOOCH_3$ (▲) during CH_3OH–O_2 reactions at 373 K on 1.0 wt% Pt/SiO_2 catalyst (3.0 nm mean Pt cluster diameter) as a function of methanol conversion with O_2/CH_3OH feed mixtures of 0.25 (a), 1.5 (b), and 16.0 (c) (4.2×10^7–2.5×10^8 cm^3 $(g_{cat}\ h)^{-1}$, 200 SiO_2-to-catalyst intra-particle and 5700 SiO_2-to-catalyst inter-particle dilution ratios).

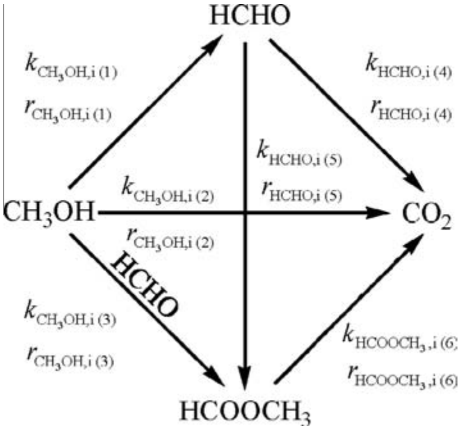

Scheme 1. Primary and secondary pathways for CH_3OH–O_2 reactions on Pt clusters.

where subscripts P, i, and (n) in $k_{p,i(n)}$ denote reductant species P, Kinetic Regime i ($i = 1, 2$, or 3), and pathway (n) ($n = 1$–6) in Scheme 1, and $[P]$ refers to the pressure of reductant P ($P = CH_3OH$, HCHO, or $HCOOCH_3$) used in the probed reactions (e.g., HCHO in HCHO–O_2 or $HCOOCH_3$ in $HCOOCH_3$–O_2 reactions). These rate constants ($k_{p,i(n)}$) were derived from rates measured in CH_3OH–O_2, HCHO–O_2, and $HCOOCH_3$–O_2 mixtures on 1.0 wt% Pt/SiO_2 (3.0 nm mean Pt cluster diameter) at 373 K and 1.26×10^8 cm^3 $(g_{cat}\ h)^{-1}$ and their values are summarized in Table 2.

HCHO–O_2 reactions did not form $HCOOCH_3$ and $HCOOCH_3$–O_2 reactions did not lead to HCHO or CH_3OH at detectable concentrations (detection limit of 5 ppmv) at all O_2 pressures at 373 K {0.13 kPa HCHO, 0.6 kPa $HCOOCH_3$, 0.1–40 kPa O_2, 1.26×10^8 cm^3 $(g_{cat}\ h)^{-1}$}. Thus, rate constants $k_{HCHO,i(5)}$ must be negligible and Reaction Pathway (5) in Scheme 1 is kinetically insignificant in all regimes (Regimes 1, 2, and 3). Rates and pseudo-first-order rate constants for secondary reactions in Regime 1 ($k_{p,1(n)} = k_{HCOOCH_3,1(6)}$ or $k_{HCHO,1(4)}$) were obtained from $HCOOCH_3$–O_2 ($k_{HCOOCH_3,1(6)}$) and HCHO–O_2 ($k_{HCHO,1(4)}$) reactions at a low O_2 pressure (0.5 kPa) and shown in Table 2. The rate constants for the secondary $HCOOCH_3$ and HCHO oxidation ($k_{HCOOCH_3,1(6)}$ and $k_{HCHO,1(4)}$, respectively) were found to be 3.8 and 4.7 mol CO_2 (g atom $Pt_{surface}$ s kPa)$^{-1}$, respectively, at 373 K. The $k_{HCOOCH_3,1(6)}$ value translates to a rate ratio for CO_2 formation from sequential $HCOOCH_3$ oxidation to those from methanol oxidation $\left(r_{HCOOCH_3,1(6)}\left(r_{CO_2,1}\right)^{-1}\right)$, where $r_{CO_2,1}$ refers to the rate of CO_2 formation from CH_3OH–O_2 reactions and subscript 1 denotes Kinetic Regime 1) of <0.01 at the low CH_3OH conversions (<3%) used in this study (373 K, Table 2). The $k_{HCHO,1(4)}$ value corresponds to a rate ratio for CO_2 formation from sequential HCHO oxidation to those from methanol oxidation $\left(r_{HCHO,1(4)}\left(r_{CO_2,1}\right)^{-1}\right)$ of <0.02 under similar conditions. These results confirm that rate contributions from secondary reactions are insignificant in Regime 1, consistent with carbon selectivities that do not vary with CH_3OH conversions and residence times in this regime (Fig. 3a). Thus, CO_2, HCHO, and $HCOOCH_3$ are formed directly from CH_3OH derived intermediates at low O_2-to-CH_3OH ratios (<0.5), as also reported previously [5].

As O_2-to-CH_3OH ratios increased to 0.5–10, the rate constant for $HCOOCH_3$ oxidation ($k_{HCOOCH_3,2(6)}$) remained at a small value {3.8 mol CO_2 (g atom $Pt_{surface}$ s kPa)$^{-1}$, 373 K}. The rate constants for the primary CH_3OH–O_2 reaction to HCHO ($k_{CH_3OH,2(1)}$) and the sequential HCHO–O_2 reaction to CO_2 ($k_{HCHO,2(4)}$), however, both increased to magnitudes similar to each other {19–38 mol HCHO (g atom $Pt_{surface}$ s kPa)$^{-1}$ and 33.7 mol CO_2 (g atom $Pt_{surface}$ s kPa)$^{-1}$, respectively, 373 K}. These rate constant values corresponded to a rate ratio for CO_2 formation from HCHO over CO_2 formation from CH_3OH, $r_{HCHO,2(4)}\left(r_{CO_2,2}\right)^{-1}$ (where $r_{CO_2,2}$ denotes the rate of CO_2 formation from CH_3OH–O_2 reactions in Kinetic Regime 2), of 0.06 to 0.14 in Regime 2 {1–2 kPa CH_3OH, 0.5–5 kPa O_2, 0.02–0.14 kPa HCHO (produced from CH_3OH–O_2 reactions), 373 K}. At even higher O_2-to-CH_3OH ratios (10–45; Regime 3), rate constants for all CH_3OH oxidation reactions ($k_{CH_3OH,3(1)}$, $k_{CH_3OH,3(2)}$, $k_{CH_3OH,3(3)}$) and HCHO oxidation ($k_{CH_3OH,3(4)}$) increased to even larger values, except those for $HCOOCH_3$ oxidation ($k_{HCOOCH_3,3(6)}$) and for the conversion of HCHO to $HCOOCH_3$ ($k_{HCHO,3(5)}$), which remained insignificant. These increases reflect the creation of active sites that are more effective for CH_3OH and HCHO oxidation at the high O_2-to-CH_3OH ratios. Comparing the rate constant values of Regime 3 with those of Regime 2, the rate constant for HCHO oxidation to CO_2 ($k_{HCHO,3(4)}$) increased to a much larger extent than the rate constants for primary reactions ($k_{CH_3OH,3(1)}$, $k_{CH_3OH,3(2)}$, $k_{CH_3OH,3(3)}$) (Table 2). This increase resulted in a concomitant decrease in HCHO selectivity and led the rate ratios for CO_2 formation from HCHO to the overall CO_2 formation from methanol oxidation $r_{HCHO,3(4)}\left(r_{CO_2,3}\right)^{-1}$, where $r_{CO_2,3}$ denotes the rate of CO_2 formation from CH_3OH–O_2 reactions in Regime 3} to exceed 0.3 in Regime 3 {0.08–2 kPa CH_3OH, 10–70 kPa O_2, 0.01–0.3 kPa HCHO (produced from CH_3OH–O_2 reaction), 373 K}. Taken together, these data indicate that sequential $HCOOCH_3$ oxidation to CO_2 does not occur at any significant extent under all O_2-to-CH_3OH ratios examined in this report. The sequential HCHO oxidation to CO_2, however, becomes increasingly important as the O_2-to-CH_3OH ratio increases from Regime 1 to Regime 3, during which the rate ratio $r_{HCHO,i(4)}\left(r_{CO_2,i}\right)^{-1}$ increases from less than 0.02 to 0.45 (Table 2).

These different trends of carbon selectivities with CH_3OH conversion and their different values when extrapolating to zero conversion (22.4% CO_2, 65.4% HCHO, and 12.2% $HCOOCH_3$ in Regime 1, 18.6% CO_2, 74.4% HCHO, and 7.0% $HCOOCH_3$ in Regime 2, and 18.1% CO_2, 74.0% HCHO, and 7.9% $HCOOCH_3$ in Regime 3; the error in carbon selectivities is <0.5%), as shown in Fig. 3, indicate that the relative contributions of primary and secondary reactions and the rate dependencies for CO_2, HCHO, and $HCOOCH_3$ formation vary

Table 2

Pseudo-first-order rate constants ($k_{p,i(n)} = r_{p,i(n)}[P]^{-1}$) and rate ratios of primary and secondary reactions for CH_3OH–O_2 reactions on 1.0 wt% Pt/SiO_2 catalysts (3.0 nm mean Pt cluster diameter) at 373 K in three different kinetic regimes, defined by the operating O_2-to-CH_3OH ratio.

Kinetic Regime i	O_2/CH_3OH Ratio	$k_{CH_3OH,i(1)}$ ^{a}	$k_{CH_3OH,i(2)}$ ^{b}	$k_{CH_3OH,i(3)}$ ^{c}	$k_{HCHO,i(4)}$ $^{\#}$	$k_{HCHO,i(5)}$ $^{\&}$	$k_{HCOOCH_3,i(6)}$ *	$r_{HCHO,i(4)}\left(r_{CO_2,i}\right)^{-1}$	$r_{HCOOCH_3,i(6)}\left(r_{CO_2,i}\right)^{-1}$
1	0.01–0.5	0.3–2.7	0.1–0.9	0.1–0.2	4.7	b.d.	3.8	<0.02	<0.01
2	0.5–10	19.0–38.0	4.9–10.0	2.1–2.4	33.7	b.d.	3.8	0.06–0.14	<0.01
3	10–45	160.9	48.0–34.0	13.8–45.3	162.0	b.d.	b.d.	0.30-0.45	<0.01

Subscripts P, i, and (n) in pseudo-first-order rate constants ($k_{p,i(n)}$) denote reductant identity P ($P = CH_3OH$, HCHO, $HCOOCH_3$), Kinetic Regime i ($i = 1, 2, 3$), and pathway (n) ($n = 1$–6 in Scheme 1). $r_{p,i(n)}$ denotes the rate of reaction pathway (n) for reductant P in Regime i and $r_{CO_2,i}$ denotes the rate of CO_2 formation during CH_3OH–O_2 reactions in Regime i. $[P]$ refers to the partial pressure of reductant P. ^{a,b,c}: Pseudo-first-order rate constants ($k_{CH_3OH,i(n)}$, ^{a}mol HCHO (g atom $Pt_{surface}$ s kPa)$^{-1}$, ^{b}mol CO_2 (g atom $Pt_{surface}$ s kPa)$^{-1}$, ^{c}mol $HCOOCH_3$ (g atom $Pt_{surface}$ s kPa)$^{-1}$) were measured from CH_3OH–O_2 reactions (0.08–5.0 kPa CH_3OH and 0.1–70 kPa O_2). $^{\#,\&}$: Pseudo-first-order rate constants ($k_{HCHO,i(n)}$, $^{\#}$mol CO_2 (g atom $Pt_{surface}$ s kPa)$^{-1}$, $^{\&}$mol $HCOOCH_3$ (g atom $Pt_{surface}$ s kPa)$^{-1}$) were measured from HCHO–O_2 reactions (0.13 kPa HCHO and 0.5 kPa, 1.5 kPa, and 16.0 kPa O_2 for Regimes 1, 2, and 3, respectively); b.d. denotes below detectable limits. *Pseudo-first-order rate constants ($k_{HCOOCH_3,i(6)}$, mol CO_2 (g atom $Pt_{surface}$ s kPa)$^{-1}$) were measured from the $HCOOCH_3$–O_2 reactions (0.60 kPa $HCOOCH_3$ and 0.1–40 kPa O_2). (200 SiO_2-to-catalyst intra-particle and 5700 SiO_2-to-catalyst inter-particle dilution ratios, 1.26×10^8 cm^3 $(g_{cat}\ h)^{-1}$).

with reactant and product pressures. Next, we probe the effects of reactant pressure on the individual rates of HCHO, $HCOOCH_3$, and CO_2 formation by varying the O_2 and CH_3OH pressures independently while maintaining a constant temperature and space velocity (373 K, 1.26×10^8 cm^3 $(g_{cat}\ h)^{-1}$ for Regimes 2 and 3 and 4.2×10^7 cm^3 $(g_{cat}\ h)^{-1}$ for Regime 1).

3.3. Diverse kinetic dependencies during methanol partial oxidation and their connection to oxygen-to-methanol ratio and the identity and coverages of reactive intermediates on Pt cluster surfaces

Fig. 4 shows the diverse rate dependencies for the formation of primary (HCHO) and secondary ($HCOOCH_3$ and CO_2) products during CH_3OH–O_2 reactions on Pt clusters (1.0 wt% Pt/SiO_2, 3.0 nm mean Pt cluster diameter, 373 K), plotted in terms of the first-order rate coefficients, defined as the turnover rates for species j (j = HCHO, $HCOOCH_3$, or CO_2) formation divided by CH_3OH pressure ($r_{j,i}$ $[CH_3OH]^{-1}$, i = Regime 1, 2, or 3), as a function of O_2-to-CH_3OH ratio. First-order rate coefficients for HCHO, $HCOOCH_3$, and CO_2 formation are a single-valued function of O_2-to-CH_3OH ratio and their rate dependencies depend strictly on the range of operating O_2-to-CH_3OH ratios, which defines the operating boundaries for Kinetic Regimes 1 to 3 in the order of increasing O_2-to-CH_3OH ratio (Regime 1: 0.01–0.5 O_2/CH_3OH, Regime 2: 0.5–10 O_2/CH_3OH, and Regime 3: 10–45 O_2/CH_3OH), irrespective of individual CH_3OH and O_2 pressure values.

The rate of species j (j = HCHO, $HCOOCH_3$, or CO_2) formation (per exposed Pt atom) in Kinetic Regime i (i = 1, 2, or 3) is denoted as $r_{j,i}$ and expressed in a general form below to vary with the CH_3OH and O_2 pressures ($[CH_3OH]$ and $[O_2]$):

$$r_{j,i} = k_{eff,j,i}[CH_3OH]^{\alpha_{j,i}}[O_2]^{\beta_{i,j}} \tag{3}$$

$$j = HCHO, HCOOCH_3, \text{ or } CO_2$$

$$i = \text{Kinetic Regime } 1, 2, \text{ or } 3$$

where $k_{eff,j,i}$ is the effective rate constant for species j, and $\alpha_{j,i}$ and $\beta_{j,i}$ are the apparent reaction orders with respect to CH_3OH and O_2, respectively, in Regime i. The formation of a HCHO, CO_2, or $HCOOCH_3$ molecule each requires one catalytic CH_3OH sojourn in the oxidative dehydrogenation step (ODH); thus, the rates of oxidative dehydrogenation of CH_3OH, $r_{ODH,i}$ (for Regime i), are reported as the combined rates of HCHO, CO_2, and $HCOOCH_3$ formation ($r_{ODH,i} = r_{HCHO,i} + r_{CO_2,i} + r_{HCOOCH_3,i}$ for Regime i) [12]. As shown

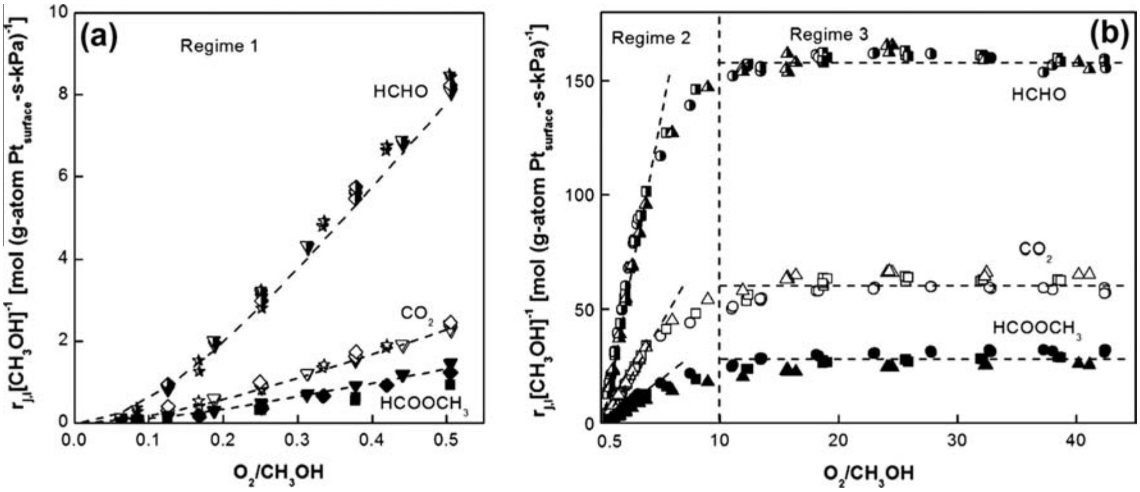

Fig. 4. 4a and 4b. First-order rate coefficients ($r_{j,i}$ $[CH_3OH]^{-1}$) for HCHO (◭, ◧, ◐, ⬖, ⯪, ⧩), CO_2 (Δ, □, ○, ◇, ☆, ▽), and $HCOOCH_3$ (▲, ■, ●, ♦, ★, ▼) formation as single-valued functions of O_2-to-CH_3OH ratio during CH_3OH–O_2 reactions at 373 K with 1.00 kPa (◭, Δ, ▲), 1.25 kPa (◧, □, ■), 1.75 kPa (◐, ○, ●), 2.00 kPa (⬖, ◇, ♦), 3.00 kPa (⯪, ☆, ★), and 4.00 kPa (⧩, ▽, ▼) of CH_3OH on 1.0 wt% Pt/SiO_2 (3.0 nm mean Pt cluster diameter, 200 SiO_2-to-catalyst intra-particle and 5700 SiO_2-to-catalyst inter-particle dilution ratios; 4.2×10^7 cm^3 $(g_{cat}\ h)^{-1}$ (4a) and 1.26×10^8 cm^3 $(g_{cat}\ h)^{-1}$ (4b). Regime 1: O_2/CH_3OH = 0.01–0.5; Regime 2: O_2/CH_3OH = 0.5–10; Regime 3: O_2/CH_3OH = 10–45).

Table 3
Identity of the most abundant surface intermediates, observed rate dependencies, and apparent reaction orders for oxidative dehydrogenation of CH_3OH and for HCHO, CO_2, and $HCOOCH_3$ formation, and the rate expressions for HCHO (primary product) formation derived from proposed elementary steps for CH_3OH–O_2 reactions on 1.0 wt% Pt/SiO_2 catalyst in Kinetic Regimes 1–3.

Kinetic Regime i	Regime 1^c (0.01 < O_2/CH_3OH < 0.5)	Regime 2^b (0.5 < O_2/CH_3OH < 10)	Regime 3^a (10 < O_2/CH_3OH < 45)
MASI$^{\#}$	$[CH_3O^*]$	$[^*]$	$[O^*]$
$r_{j,i}$	$k_{eff,j,1}[CH_3OH]^{\alpha_{j,1}}[O_2]^{\beta_{j,1}}$	$k_{eff,j,2}[CH_3OH]^{\alpha_{j,2}}[O_2]^{\beta_{j,2}}$	$k_{eff,j,3}[CH_3OH]^{\alpha_{j,3}}[O_2]^{\beta_{j,3}}$
$r_{ODH,i}$	$k_{eff,ODH,1}[CH_3OH]^{-0.7}[O_2]^{1.7}$	$k_{eff,ODH,2}[O_2]$	$k_{eff,ODH,3}[CH_3OH]$
$r_{HCHO,i}$	$k_{eff,HCHO,1}[CH_3OH]^{-0.7}[O_2]^{1.7}$	$k_{eff,HCHO,2}[O_2]$	$k_{eff,HCHO,3}[CH_3OH]$
$r_{CO_2,i}$	$k_{eff,CO_2,1}[CH_3OH]^{-0.7}[O_2]^{1.7}$	$k_{eff,CO_2,2}[CH_3OH]^{-0.2}[O_2]$	$k_{eff,CO_2,3}[CH_3OH]^{0.8}$
$r_{HCOOCH_3,i}$	$k_{eff,HCOOCH_3,1}[O_2]^2$	$k_{eff,HCOOCH_3,2}[CH_3OH]^{0.3}[O_2]^{1.4}$	$k_{eff,HCOOCH_3,3}[CH_3OH]^{1.4}$
$r_{HCHO,i}$ derived from proposed elementary steps	$\frac{k_{1.5}}{k_{1.5}+k_{1.6}}\frac{k_{1.3}K_{1.2}[CH_3OH]}{\left(1+\frac{k_{1.3}K_{1.2}[CH_3OH]}{k_{1.4}K_{1.1}[O_2]}\right)^2}$	$\frac{2k_{2.1}k_{2.5}[O_2]}{k_{2.5}+k_{2.6}} - \frac{k_{2.6}k_{2.5,r}[HCHO]}{k_{2.5}+k_{2.6}}$	$\frac{k_{3.3}k_{3.5}[CH_3OH]}{k_{3.5}+k_{3.6}} - \frac{k_{3.6}k_{3.5,r}[HCHO]}{k_{3.5}+k_{3.6}}$

^{a,b}: 1.26×10^8 cm^3 $(g_{cat}\ h)^{-1}$; ^{c}: 4.2×10^7 cm^3 $(g_{cat}\ h)^{-1}$. ^{a,b,c}: 373 K, 3.0 nm mean Pt cluster diameter, 200 SiO_2-to-catalyst intra-particle and 5700 SiO_2-to-catalyst inter-particle dilution ratios. $^{\#}$MASI denotes the most abundant surface intermediates. The subscripts j, i in rates ($r_{j,i}$, mol (g atom $Pt_{surface}$ s)$^{-1}$), effective rate constants ($k_{eff,j,i}$, mol (g atom $Pt_{surface}$ s kPa)$^{-1}$), and apparent reaction orders ($\alpha_{j,i}$ and $\beta_{j,i}$) denote carbon-containing products j (j = HCHO, CO_2, $HCOOCH_3$) and Kinetic Regime i (i = 1, 2, 3). Subscript ODH denotes oxidative dehydrogenation of CH_3OH.

in Table 3, the rate dependencies for the individual rates of HCHO, CO_2, and $HCOOCH_3$ formation ($\alpha_{j,i}$ and $\beta_{j,i}$) differ from one regime to another.

For O_2-to-CH_3OH ratios above 10, the rates for HCHO, $HCOOCH_3$, and CO_2 formation are independent of O_2 pressure ($\beta_{HCHO,3} = \beta_{HCOOCH_3,3} = \beta_{CO_2,3} = 0 \pm 0.1$). These rates with respect to CH_3OH pressure are first-order for HCHO formation ($\alpha_{HCHO,3} = 1 \pm 0.02$), less than first-order for CO_2 formation ($\alpha_{CO_2,3} = 0.8 \pm 0.01$), and larger than first-order for $HCOOCH_3$ formation ($\alpha_{HCOOCH_3,3} = 1.4 \pm 0.1$). As the O_2-to-CH_3OH ratio decreases to below 10 but above 0.5, the transition from Regime 3 to Regime 2 occurs, during which the reaction orders with respect to O_2 for HCHO and CO_2 formation increase from zero to one ($\beta_{HCHO,2} = 1.1 \pm 0.1, \beta_{CO_2,2} = 1.1 \pm 0.1$) and for $HCOOCH_3$ from zero to ~ 1.5 ($\beta_{HCOOCH_3,2} = 1.4 \pm 0.2$), while those with respect to CH_3OH for HCHO and CO_2 formation concomitantly decrease from one to near zero values ($\alpha_{HCHO,2} = 0 \pm 0.1$, $\alpha_{CO_2,2} = -0.2 \pm 0.1$) and for $HCOOCH_3$ formation from larger than one to near 0.5 ($\alpha_{HCOOCH_3,2} = 0.3 \pm 0.1$). A further decrease in O_2-to-CH_3OH ratio to less than 0.5 leads to another transition in reaction orders, during which the rates for HCHO and CO_2 formation ($r_{HCHO,1}$ and $r_{CO_2,1}$) both acquire an even stronger positive dependence with O_2 ($\beta_{HCHO,1} = \beta_{CO_2,1} = 1.7 \pm 0.2$) and a negative dependence with CH_3OH ($\alpha_{HCHO,1} = \alpha_{CO_2,1} = -0.7 \pm 0.2$) while the rates for $HCOOCH_3$ formation depend solely on O_2 pressure ($\beta_{HCOOCH_3,1} = 2 \pm 0.2$) and are no longer vary with CH_3OH pressure ($\alpha_{HCOOCH_3,1} = 0 \pm 0.1$). These effects of O_2-to-CH_3OH ratios on the individual species formation rates are captured in Fig. 4a (for Regime 1) and 4b (for Regimes 2 and 3) and their effects on the carbon selectivities are shown in Fig. 5a (for Regime 1) and 5b (for Regimes 2 and 3).

In the next sections (Sections 3.4-3.6), we provide the evidence that the increase in reaction orders with respect to O_2 ($\beta_{j,3} < \beta_{j,2} < \beta_{j,1}$) and the concomitant decrease in reaction orders with respect to CH_3OH ($\alpha_{j,3} > \alpha_{j,2} > \alpha_{j,1}$) from Regime 3 to Regime 1, as summarized in Table 3, are caused by a decrease in oxygen chemical potential at Pt cluster surfaces. The decrease in oxygen chemical potential results in a dynamic transition in the coverages of reactive intermediates from saturated with chemisorbed oxygen atoms (O^*) (Regime 3), uncovered of (Regime 2), to covered with methanol derived species (Regime 1). A sequence of elementary steps for methanol and oxygen activation, HCHO formation, and sequential HCHO oxidation is proposed in Scheme 2. Elementary steps for HCHO, CO_2, $HCOOCH_3$, and H_2O formation in Regimes 3, 2, and 1 are provided in Schemes A.1, A.2, and A.3 respectively. These elementary reaction steps in Schemes 2 and A.1-A.3 may occur concurrently in all regimes, but their relative contributions to the observed rates differ markedly, because of the difference in site abundances of chemisorbed oxygen atoms (O^*), unoccupied Pt sites (*), and methanol derived species (e.g., CH_3O^*) and the extent of their participation in catalysis from one regime to another. In Scheme 2, the dominant reaction steps for each regime are presented. During the transition from one regime to another, the elementary rate constant and equilibrium constant values are expected to vary with changes in surface coverages, lateral repulsive interactions, and heats of adsorption. We focus next on analyzing the individual regimes, starting from the highest O_2-to-CH_3OH ratios (10–45), which correspond to Kinetic Regime 3, at which Pt cluster surfaces are saturated with chemisorbed oxygen atoms that assist with the initial CH_3OH activation and HCHO oxidation steps.

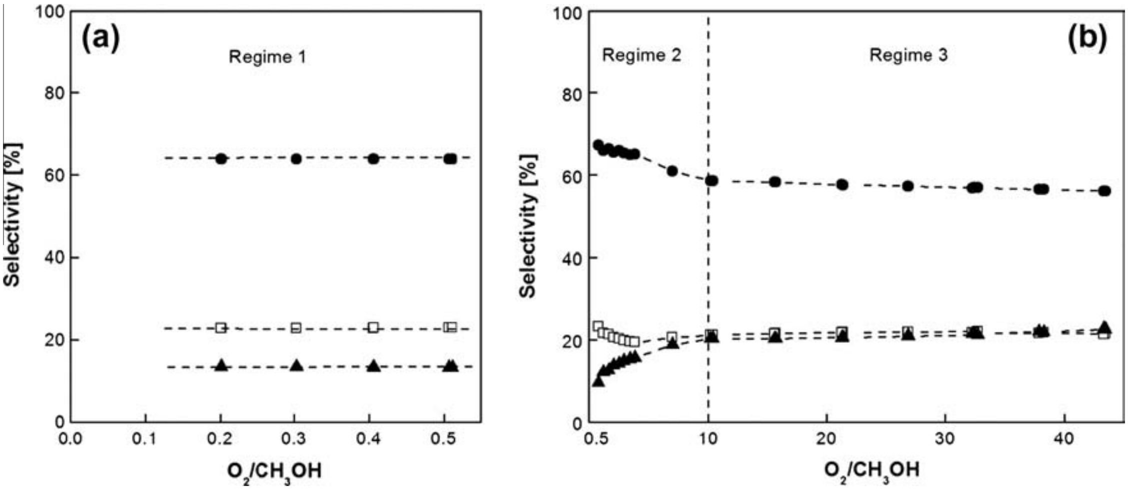

Fig. 5. 5a and 5b. Effects of O_2-to-CH_3OH ratio on carbon selectivities toward HCHO (●), CO_2 (□), and $HCOOCH_3$ (▲) during CH_3OH-O_2 reactions on 1.0 wt% Pt/SiO_2 catalyst at 373 K (3.0 nm mean Pt cluster diameter, 4.2×10^7 cm^3 (g_{cat} h)$^{-1}$ (5a) and 1.26×10^8 cm^3 (g_{cat} h)^{1} (5b), 1.50 kPa CH_3OH, 200 SiO_2-to-catalyst intra-particle and 5700 SiO_2-to-catalyst inter-particle dilution ratios).

	Regime 1		Regime 2		Regime 3
Step *i.s*	Elementary reaction step	Step *i.s*	Elementary reaction step	Step *i.s*	Elementary reaction step
1.1	$O_2 + * \longleftrightarrow O_2^*$	2.1	$O_2 + 2* \longrightarrow 2O^*$	3.1	$O_2 + 2* \longrightarrow 2O^*$
1.2	$CH_3OH + * \longleftrightarrow CH_3OH^*$	2.2	$CH_3OH + * \longleftrightarrow CH_3OH^*$	3.3	$CH_3OH + 2O^* \longrightarrow CH_3OO^* + OH^*$
1.3	$CH_3OH^* + * \longrightarrow CH_3O^* + H^*$	2.3	$CH_3OH^* + O^* \longleftrightarrow CH_3O^* + OH^*$	3.4	$CH_3OO^* + O^* \longrightarrow CH_2O_2^* + OH^*$
1.4	$CH_3O^* + O_2^* \longrightarrow CH_2O_2^* + OH^*$	2.4	$CH_3O^* + O^* \longrightarrow CH_2O^* + OH^*$	3.5	$CH_2O_2^* \rightleftharpoons HCHO + O^*$
1.5	$CH_2O_2^* + * \longrightarrow HCHO^* + O^*$	2.5	$CH_2O^* \rightleftharpoons HCHO + *$	3.6	$CH_2O_2^* + O^* \longrightarrow HCO_2^* + OH^*$
1.6	$CH_2O_2^* + * \longrightarrow HCO_2^* + H^*$	2.6	$CH_2O^* + * \longrightarrow CHO^* + H^*$		

(* refers to an unoccupied Pt site, $\longrightarrow$ denotes an irreversible step, $\longleftrightarrow$ a quasi-equilibrated step, and $\rightleftharpoons$ a reversible step; $k_{i,s}$ and $k_{i,s,r}$ are the forward and reverse rate constants of Step *s* in Kinetic Regime *i*, and $K_{i,s}$ is the equilibrium constant for Step *s* in Kinetic Regime *i*.)

Scheme 2. A proposed sequence of elementary steps for HCHO formation from CH_3OH and O_2 reactions on Pt clusters.

3.4. Methanol partial oxidation on Pt cluster surfaces saturated with chemisorbed oxygen atoms (Regime 3)

HCHO, $HCOOCH_3$, and CO_2 formation rates from CH_3OH–O_2 mixtures were measured on 1.0 wt% Pt/SiO_2 (3.0 nm mean Pt cluster diameter) at 373 K by independently varying the CH_3OH and O_2 pressures from 0.08 to 1.75 kPa and 10 to 70 kPa, respectively, while maintaining the O_2-to-CH_3OH ratio at values between 10 and 45. The species formation rates ($r_{j,3}$, subscript j denotes HCHO, CO_2, or $HCOOCH_3$ and subscript 3 denotes Regime 3), are shown as a function of CH_3OH pressure (0.08–1.5 kPa) in Figs. 6a, A.1a, and A.1b, respectively, for three different O_2 pressures of 20, 28, and 35 kPa and their rate dependencies with CH_3OH and O_2 ($r_{j,3} = k_{\mathrm{eff},j,3}[CH_3OH]^{\alpha_{j,3}}[O_2]^{\beta_{j,3}}$) are summarized in Table 3. Turnover rates for HCHO, CO_2, and $HCOOCH_3$ formation increase with CH_3OH pressure with apparent reaction orders $\alpha_{HCHO,3}$, $\alpha_{CO_2,3}$, and $\alpha_{HCOOCH_3,3}$ of 1.0 ± 0.02, 0.8 ± 0.01, and 1.4 ± 0.1, respectively. These rates do not vary with O_2 pressure ($\beta_{j,3} = 0 \pm 0.1$, j = HCHO, $HCOOCH_3$, or CO_2). Previous studies also reported similar rate dependencies for HCHO formation during CH_3OH–O_2 reactions at high O_2-to-CH_3OH ratios on Ag (2.5–20 O_2/CH_3OH, 563–593 K) [5], RuO_2 (2.5–7 O_2/CH_3OH, 393 K) [12], and $Fe_2(MoO_4)_3$ (5–40 O_2/CH_3OH, 433 K) [16]. Despite the similar rate dependencies for Pt and other metal (Ag [5]) or metal oxide (RuO_2 [12] and $Fe_2(MoO_4)_3$ [16]) structures, the previously proposed mechanism [12,16], which requires competitive adsorption of CH_3OH and O_2 on unoccupied metal sites or oxygen vacancies (*), is not consistent with the zero-order dependence of HCHO formation rates on O_2 pressure in this regime. The zero-order dependence of all rates (for the formation of primary and secondary products) on O_2 pressure indicates that O_2 activation step is kinetically insignificant at these high O_2-to-CH_3OH ratios. Thus, Pt cluster surfaces must be saturated with reactive oxygen atoms at surfaces (or subsurfaces). The active site structures formed with these oxygen atoms do not vary with oxygen chemical potential and the accessibility to unoccupied metal or oxygen vacancy sites does not limit CH_3OH turnovers in this regime. CH_3OH activation did not occur at exposed Pt sites used for binding the reactive oxygen atoms, because if it did, an increase in O_2 pressure would deplete the concentration of unoccupied Pt sites and lead to lower CH_3OH activation rates. In this specific case, rates for CH_3OH conversion and for HCHO, $HCOOCH_3$, and CO_2 formation would acquire a negative dependence on O_2 pressure.

These kinetic evidence (Figs. 6a, A.1a, and A.1b) led us to propose a sequence of elementary steps involving irreversible dissociation of O_2 molecules on Pt sites and activation of CH_3OH on O* covered Pt cluster surfaces. The reversibility of the O_2 dissociation step is given by the relative magnitudes for the rates of O* recombination (also the reverse step of O_2 dissociation on Pt sites) and those of O* removal by reaction with CH_3OH. The rates of O* recombination on O* saturated Pt cluster surfaces have been previously measured from $^{16}O^{18}O$ isotopologue formation in $^{16}O_2$–$^{18}O_2$ mixtures [44,45]. $^{16}O^{18}O$ isotopologue formation rates from $^{16}O_2$–$^{18}O_2$ reactions were undetectable and estimated to be lower than 2.5×10^{-3} mol O_2 (g atom surface Pt s)$^{-1}$ (20 kPa of 1:1 $^{16}O_2$–$^{18}O_2$ mixture) on O* covered Pt clusters at a higher temperature of 473 K [44]. Extrapolation of the $^{16}O^{18}O$ isotopologue formation rates on O* covered Pt surfaces from a higher temperature range (2 kPa of 1:1 $^{16}O_2$–$^{18}O_2$ mixtures; activation barrier: 108 kJ mol^{-1}; 550–715 K [45]) to 373 K gave an $^{16}O^{18}O$ formation rate of 1.2×10^{-8} mol O_2 (g atom surface Pt s)$^{-1}$ at 65 kPa O_2. These O* recombination rates ($r_{O_{16}O_{18}}$) are significantly lower than the CH_3OH forward chemical turnovers with an estimated rate ratio for oxygen recombination to CH_3OH oxidative dehydrogenation, $r_{O_{16}O_{18}}(r_{ODH,3})^{-1}$, of $<10^{-10}$ at 373 K (0.08 kPa CH_3OH, 65 kPa O_2). Thus, the O_2 dissociation step must be irreversible during CH_3OH oxidation in this regime and is expected to remain even more so on Pt cluster surfaces depleted of O* (Regimes 2 and 1 in Sections 3.5 and 3.6, respectively) as the probability of O* atoms to recombine and desorb as O_2 decreases markedly with decreasing O* coverages. Chemisorbed oxygen atoms must involve in CH_3OH activation, because of much larger rates on O* saturated surfaces (Regime 3) than on cluster surfaces sparse of reactive oxygen species (Regimes 2 and 1, Fig. 4). On O* saturated surfaces, CH_3OH must activate over chemisorbed oxygen atoms as the active sites, possibly via the cleavage of its O–H bond.

In this regime, the coverages of CH_3OH derived intermediates (e.g., CH_3O^*) must be insignificant, because site occupation by these intermediates would lead the rates for HCHO ($r_{HCHO,3}$, Fig. 6a) and the combined rates for secondary product ($r_{CO_2,3} + r_{HCOOCH_3,3}$, Fig. 6b) formation to increase less than linearly with CH_3OH pressure. We note that the identity of carbon-contain-

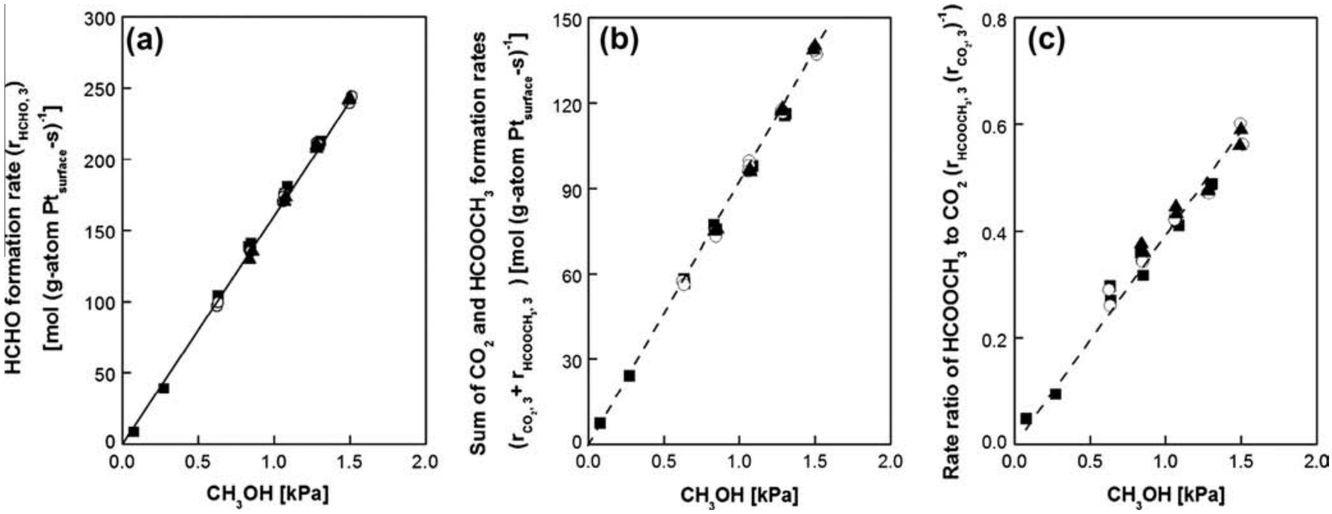

Fig. 6. (a) HCHO formation rates ($r_{HCHO,3}$) {—: predicted values from linear regression of rate data with Eq. (6)}, (b) sum of CO_2 and $HCOOCH_3$ formation rates ($r_{CO_2,3} + r_{HCOOCH_3,3}$), and (c) rate ratio of $HCOOCH_3$ to CO_2 ($r_{HCOOCH_3,3}(r_{CO_2,3})^{-1}$) as a function of CH_3OH pressure during CH_3OH–O_2 reactions with 20.0 kPa (■), 28.0 kPa (○) and 35.0 kPa (Δ) of O_2 on 1.0 wt% Pt/SiO_2 (3.0 nm mean Pt cluster diameter) at 373 K. (1.26×10^8 cm^3 (g_{cat} h)$^{-1}$, 200 SiO_2-to-catalyst intra-particle and 5700 SiO_2-to-catalyst inter-particle dilution ratios).

ing intermediates derived from CH_3OH activation at high O^* coverages is difficult to identify and remain essentially invisible from spectroscopic studies, because of their low coverages during steady-state reactions. In addition, attempts to probe these species on well-defined Pt single-crystal surfaces are limited by their inherent constraint to attain saturation O^* coverages (e.g., the maximum O^* coverages were found to be less than 0.25 ML on Pt(1 1 1) at 300 K [28,36]). The lack of significant and detectable coverages of CH_3OH derived intermediates was confirmed from chemical titration of carbon-containing debris on Pt cluster surfaces using O_2 as titrants, carried out after steady-state CH_3OH–O_2 reactions in this regime for 1 h (O_2/CH_3OH = 16, 373 K, 4.2×10^7 cm^3 (g_{cat} - h)$^{-1}$). The expected chemical titration products (CO_2 or CO) were not detected from these studies within the detection limits. Taken together the rate dependencies (Fig. 6a and b, A.1a, and A.1b) and titration results, Pt cluster surfaces must be free of CH_3OH derived intermediates in this regime.

These results led us to propose that the kinetically-relevant step must involve initial CH_3OH activation assisted by reactive oxygen atoms, which saturate the Pt cluster surfaces, followed by sequential hydrogen abstraction to form the $CH_2O_2^*$ species, as shown in Scheme 2. Desorption of $CH_2O_2^*$ leads to HCHO [5,25] and leaves behind a chemisorbed oxygen (O^*) on Pt cluster. Alternatively, the hydrogen abstraction of $CH_2O_2^*$ species forms the formate species (HCO_2^*), which may bind to Pt surfaces at bridge or monodentate configurations [46]. The formate species may combine with another CH_3OH to evolve the $HCOOCH_3$ (leaving behind an O^*) as a secondary product [19,20], or alternatively, undergo hydrogen abstraction and desorb as CO_2 [20,25]. The net rates of HCHO formation are given by subtracting the rates of HCHO oxidation from the rates of $CH_2O_2^*$ desorption (to form HCHO and O^*):

$$r_{HCHO,3} = \frac{k_{3.5}[CH_2O_2^*]}{[T]} - \frac{k_{3.5,r}[HCHO][O^*]}{[T]} \tag{4}$$

where $k_{3.5}$ and $k_{3.5,r}$ are the forward and reverse rate constants for HCHO desorption steps, the former leads to HCHO formation and the latter to sequential oxidation, respectively, as defined in Scheme 2; $[CH_2O_2^*]$ and $[O^*]$ are the concentrations of adsorbed $CH_2O_2^*$ and O^* on platinum surface sites, respectively; [HCHO] is the partial pressure of formaldehyde during catalysis; [T] is the concentration of total sites on Pt cluster surfaces. The surface concentration of $CH_2O_2^*$, $[CH_2O_2^*]$, is obtained from kinetic coupling of rates that form (Step 3.4 and reverse reaction of Step 3.5, Scheme 2) and remove (forward reaction of Step 3.5 and Step 3.6, Scheme 2) $CH_2O_2^*$ from Pt cluster surfaces during steady-state catalysis:

$$[CH_2O_2^*] = \frac{k_{3.3}[CH_3OH][O^*]}{k_{3.5} + k_{3.6}} + \frac{k_{3.5,r}[HCHO][O^*]}{k_{3.5} + k_{3.6}} \tag{5}$$

where $k_{3.3}$ and $k_{3.6}$ are the rate constants for the initial activation of CH_3OH assisted by reactive oxygen species and the sequential hydrogen abstraction of $CH_2O_2^*$ to evolve formate (HCO_2^*), respectively. Substitution of Eq. (5) into Eq. (4) leads the HCHO formation rates ($r_{HCHO,3}$) to vary with CH_3OH and HCHO pressures (see Section A.1 in Appendix for derivation):

$$r_{HCHO,3} = \frac{k_{3.5}k_{3.3}[CH_3OH]}{k_{3.5} + k_{3.6}} - \frac{k_{3.6}k_{3.5,r}[HCHO]}{k_{3.5} + k_{3.6}} \tag{6}$$

The readsorption and sequential oxidation of HCHO may reduce the rates of HCHO formation, but the rate ratio for HCHO readsorption and sequential oxidation {2nd term of Eq. (6)} to HCHO formation {1st term of Eq. (6)} remains a constant value (estimated to be 0.18 ± 0.01 at 373 K, 1.0 wt% Pt/SiO$_2$, O_2/CH_3OH = 10–45, 1.26×10^8 cm^3 (g_{cat} h)$^{-1}$) because both the rate dependencies for HCHO oxidation and for CH_3OH conversion to HCHO are identical, i.e. independent of O_2 pressure and increases proportionally with the reductant (HCHO or CH_3OH) pressure. These rate dependencies lead the HCHO pressure and resulting HCHO oxidation rates to become proportional to CH_3OH pressure. The kinetic parameters for HCHO formation in Eq. (6) were determined from linear regression with the rate data in Fig. 6a. Their values are included in Table A.1 in Appendix, the predicted rates are included in Fig. 6a, and the parity plot for measured and estimated rates is included in Fig. A.2 in Appendix.

H abstraction on the $CH_2O_2^*$ intermediates (Step 3.6, Scheme 2) forms the formate species (HCO_2^*), a common precursor for CO_2 and $HCOOCH_3$. A majority of the formate species undergo hydrogen abstraction to evolve CO_2, while a small portion reacts with CH_3OH to evolve $HCOOCH_3$. Thus, the combined rates for CO_2 and $HCOOCH_3$ formation are proportional to the concentration of $CH_2O_2^*$ on Pt cluster surfaces, whose coverages are given by CH_3OH and HCHO pressures (Eq. (5)):

$$\begin{aligned} r_{CO_2,3} + r_{HCOOCH_3,3} &= \frac{k_{3.6}[CH_2O_2^*][O^*]}{[T]^2} \\ &= \frac{k_{3.6}k_{3.3}[CH_3OH]}{k_{3.5} + k_{3.6}} + \frac{k_{3.6}k_{3.5,r}[HCHO]}{k_{3.5} + k_{3.6}} \end{aligned} \tag{7}$$

where rate constants $k_{3.3}$, $k_{3.5}$, $k_{3.5,r}$, and $k_{3.6}$ and [T] are defined above and in Scheme 2. The combined rates for CO_2 and $HCOOCH_3$ formation ($r_{CO_2,3} + r_{HCOOCH_3,3}$) vary linearly with CH_3OH pressure, as shown in Fig. 6b. The rate ratio of $HCOOCH_3$ to CO_2 formation ($r_{HCOOCH_3,3}(r_{CO_2,3})^{-1}$) is, however, proportional to CH_3OH pressure via a proportionality constant $k_{HCO_2^*-CH_3OH}\left(k_{HCO_2^*-O^*}\right)^{-1}$ of 0.392 ± 0.003 (Fig. 6c), which equals the ratio of rate constant for $HCOOCH_3$ formation from the reaction of formate with CH_3OH ($k_{HCO_2^*-CH_3OH}$) and that for CO_2 formation from H abstraction on HCO_2^* ($k_{HCO_2^*-O^*}$), respectively, as derived in Section A.1 of Appendix. The linear dependent of $HCOOCH_3$-to-CO_2 selectivity ratio $\{r_{HCOOCH_3,3}(r_{CO_2,3})^{-1}\}$ with CH_3OH pressure is consistent with the fact that HCO_2^* forms $HCOOCH_3$ only by their reaction with another CH_3OH but forms CO_2 directly. Next, we show that the most abundant surface intermediates and the steps for CH_3OH activation undergo a concomitant dynamic transition in response to decreasing O_2-to-CH_3OH ratio to values smaller than 10.

3.5. Methanol partial oxidation on uncovered Pt cluster surfaces (Regime 2)

As O_2-to-CH_3OH ratio decreases to less than 10 but larger than 0.5, rate dependencies for HCHO, $HCOOCH_3$, and CO_2 formation undergo a concomitant transition and acquire reaction orders unlike those in Regime 3. In Regime 2, the rate dependencies for oxidative dehydrogenation of CH_3OH ($r_{ODH,2}$) are shown in Fig. 7a, the rates of HCHO ($r_{HCHO,2}$), CO_2 ($r_{CO_2,2}$), and $HCOOCH_3$ ($r_{HCOOCH_3,2}$) formation in Fig. 7b, A.3a, and A.3b, respectively, and the sum of CO_2 and $HCOOCH_3$ formation rates in Fig. 7c as a function of O_2 pressure (0.5–5 kPa) for 1.0, 1.5, and 2.0 kPa CH_3OH for CH_3OH–O_2 reactions on Pt clusters (3.0 nm mean Pt cluster diameter) at 373 K. Turnover rates for oxidative dehydrogenation of CH_3OH and for HCHO and CO_2 formation are no longer independent of but increase proportionally with O_2 pressure in this regime ($\beta_{ODH,2} = \beta_{HCHO,2} = \beta_{CO_2,2} = 1.1 \pm 0.1$, Table 3). These rates also become insensitive to CH_3OH pressure ($\alpha_{ODH,2} = 0 \pm 0.1$, $\alpha_{HCHO,2} = 0 \pm 0.1$, and $\alpha_{CO_2,2} = -0.2 \pm 0.1$, Table 3). Turnover rates for $HCOOCH_3$ formation, however, increase more than linearly with O_2 and depend weakly on CH_3OH pressure ($\beta_{HCOOCH_3,2} = 1.4 \pm 0.2$, and $\alpha_{HCOOCH_3,2} = 0.3 \pm 0.1$, Table 3). These effects of CH_3OH and O_2 pressures are consistent with O_2 activation on uncovered Pt cluster surfaces as the kinetically-relevant step. Pt cluster surfaces must be largely free of molecular debris from CH_3OH and O_2 activation, because the opposite case would lead

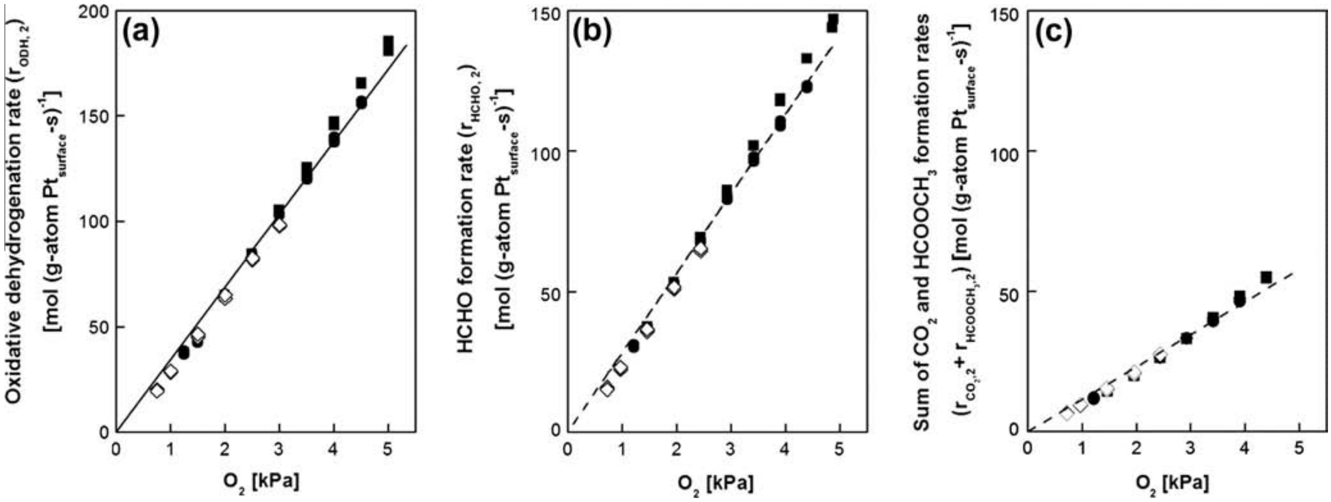

Fig. 7. (a) Oxidative dehydrogenation rates of CH_3OH {$r_{ODH,2}$, —: predicted rates of CH_3OH oxidative dehydrogenation from linear regression of rate data with Eq. (8)}, (b) rates of HCHO formation ($r_{HCHO,2}$), and (c) sum of rates for CO_2 and $HCOOCH_3$ formation ($r_{CO_2,2} + r_{HCOOCH_3,2}$) during CH_3OH–O_2 reactions with 1.0 kPa (◇), 1.5 kPa (●), and 2.0 kPa (■) of CH_3OH on 1.0 wt% Pt/SiO$_2$ (3.0 nm mean Pt cluster diameter) as a function of O_2 pressure (373 K, 1.26×10^8 cm^3 (g_{cat} h)$^{-1}$, 200 SiO$_2$-to-catalyst intra-particle and 5700 SiO$_2$-to-catalyst inter-particle dilution ratios).

to site occupation and O_2 activation rates that are less than first order with respect to O_2 and negative order with CH_3OH.

We propose the following steps for CH_3OH catalytic sojourns in this regime. CH_3OH first adsorbs molecularly via a quasi-equilibrated step on a Pt site through its oxygen atom (Step 2.2, Scheme 2), as proposed from chemical bonding shifts of the two higher-lying orbitals (related to the lone-pair and the O in CH_3OH) in UV photoemission spectra (UPS) during CH_3OH adsorption on Pt(1 1 1) (150–200 K) [47] and dispersion corrected density functional theory calculations on Pt(1 1 1) surfaces [48]. The adsorbed CH_3OH undergoes a series of hydrogen abstraction steps, likely assisted by O* to first cleave its O–H bond to form a methoxide intermediates (CH_3O^*; Step 2.3, Scheme 2) and then the C–H bond of CH_3O^* to form CH_2O^* (Step 2.4, Scheme 2) before its eventual desorption as HCHO [49]. The catalytic involvement of oxygen in O–H bond activation has been probed and confirmed from temperature desorption spectroscopy and high-resolution electron energy loss spectroscopy (EELS) on Pt(1 1 1) surfaces partially covered with O* at 170 K [50,51].

The O* assisted O–H bond dissociation in CH_3OH was found to be more exothermic ($CH_3OH(g) + * + O^* \rightarrow CH_3O^* + OH^*$, $\Delta H^{\circ}_{298} = -76.4$ kJ mol^{-1}) than the similar step without O* involvement ($CH_3OH(g) + * + * \rightarrow CH_3O^* + H^*$, $\Delta H^{\circ}_{298} = -4$ kJ mol^{-1}) on Pt(1 1 1) surfaces, as measured from single-crystal adsorption calorimetry (SCAC) studies [52]. The higher exothermicity is consistent with the lower activation barrier for CH_3OH activation on $*$–O* than $*$–$*$ site pairs, as predicted from the Brønsted–Evans–Polanyi relation and confirmed from temperature-programmed reactions of pre-adsorbed CH_3OD with O* (E_a = 23 kJ mol^{-1}) on 0.25 ML O* covered Pt(1 1 1) (115–140 K) [23] and CH_3OH decomposition on uncovered Pt(1 1 1) (E_a = 48 kJ mol^{-1}) [53]. Density functional theory calculations (DFT) of CH_3OH activation on Cu(1 1 0) surfaces show barrierless O–H bond dissociation with O* involvement (0.25 ML O*), but this step acquires a barrier of 41 kJ mol^{-1} without O* involvement [25,54]. DFT calculations on Cu(1 1 0) surfaces also give lower activation barriers for H abstraction on CH_3O^* when assisted by O* than by $*$ {E_a = 54 kJ mol^{-1} with O* vs. 118 kJ mol^{-1} with $*$ (without O*)} [25]. Similar oxygen assisted O–H and C–H bond activation routes are proposed for CH_3OH and C_2H_5OH activation on RuO$_2$ structures in a Mars-van Krevelen-type redox cycle [12]. The CH_3OH activation step is kinetically coupled with the O_2 dissociation step that must maintain its irreversible nature, as found for Regime 3 (Section 3.4). The irreversible nature of O_2 dissociation is confirmed from an estimated rate ratio of oxygen recombination to CH_3OH oxidative dehydrogenation {$r_{O_{16}O_{18}}(r_{ODH,2})^{-1}$} of less than 2×10^{-11} at 373 K, based on extrapolation of O* recombination rates from 550–715 K [45] to 373 K and $r_{ODH,2}$ of 200 mol CH_3OH (g atom $Pt_{surface}$ s)$^{-1}$ (at 5 kPa O_2 and 1 kPa CH_3OH). This is expected because of lower O* coverages in this regime than Regime 3 and thus much lower probabilities for an O* to encounter a neighboring O* for recombinative desorption.

These catalytic steps and the assumption of unoccupied Pt sites ($*$) as the most abundant surface intermediates ($[*] \approx [T]$, where $[*]$ denotes the surface concentration of unoccupied Pt sites and [T] the total exposed Pt sites) lead the CH_3OH oxidative dehydrogenation rates ($r_{ODH,2}$) to increase proportionally with O_2 pressure (derived in Section A.3 in Appendix):

$$r_{ODH,2} = \frac{2k_{2.1}[O_2][*]^2}{[T]^2} = 2k_{2.1}[O_2] \tag{8}$$

where $k_{2,1}$ reflects the rate constant for O_2 dissociation on Pt cluster surfaces (Step 2.1, Scheme 2), which includes a statistical factor correcting for the double counting of indistinguishable neighboring sites required for O_2 activation. CH_3OH activation is kinetically-irrelevant; thus, O–H and C–H bond cleavages in CH_3OH and their O* involvement remain kinetically invisible. Similar rate dependencies (Eq. (8)) and mechanistic conclusions on kinetically-relevant O_2 activation have also been reported for other oxidation reactions (CH_4–O_2 [39,40], CO–O_2 [40], and C_2H_6–O_2 [41] at >773 K) at high reductant and low O_2 pressures, at which the reductant effectively scavenges O* from cluster surfaces, leaving Pt sites uncovered and available for the kinetically-relevant O_2 dissociation. The measured rate constant for O_2 dissociation, $k_{2.1}$, is 20 mol O_2 (g atom $Pt_{surface}$ -s kPa)$^{-1}$ (373 K, from linear regression of rate data in Fig. 7a with Eq. (8); Table A.2 in Appendix Section A.4), a value lower than the extrapolated values of 750–800 mol O_2 (g atom $Pt_{surface}$ s kPa)$^{-1}$ from high temperatures (>773 K) in CH_4–O_2 and CO–O_2 mixtures to 373 K using the reported activation barriers {CH_4–O_2 mixtures: 5040 mol O_2 (g atom $Pt_{surface}$ s kPa)$^{-1}$ at 873 K, 3–20 kJ mol^{-1} on 1.8–8.5 nm Pt cluster [39]; CO–O_2 mixtures: 4700 mol O_2 (g atom $Pt_{surface}$ s kPa)$^{-1}$ at 773 K, 8–10 kJ mol^{-1} on 3.3 nm Pt cluster [55]}. The effective activation barrier for CH_3OH conversion, which also equals the O_2 dissociation barrier, was found to be 26 kJ mol^{-1}

(between 345 and 390 K; data not shown here), a value higher than those reported for O_2 dissociation at the much higher temperatures (3–20 kJ mol^{-1}, 773–873 K [39,55]). We speculate that a small amount of reactive intermediates (e.g., CO* and/or CH_3O^*) formed during catalysis may preferentially bind to coordinatively unsaturated corner and edge sites. DFT calculated CO* adsorption energies on a 201-atom cubo-octahedral Pt cluster are −171 kJ mol^{-1} on corner sites and −161 kJ mol^{-1} on edge sites [56], and CH_3O^* adsorption energy on these sites is estimated to be more negative than −145 kJ mol^{-1}, the value for CH_3O^* adsorption on closed packed Pt(1 1 1) surfaces [21]. Preoccupation of corner and edge sites by CO* or CH_3O^* prevents these sites to involve catalytically and thus they remain kinetically invisible, but as the temperature increases and CO* or CH_3O^* intermediates desorb, these sites become available for O_2 activation, leading to rates larger than those predicted based on the low activation energy expected for this step. Linear regression of rate data with Eq. (8) gave the predicted ODH rates in Regime 2, included in Fig. 7a as a function of O_2 pressure and plotted together with the measured rates in a parity plot in Fig. A.5 (Appendix Section A.4).

Although the overall rates of CH_3OH oxidative dehydrogenation (Fig. 7a), rates of HCHO formation (Fig 7b), and combined rates of CO_2 and $HCOOCH_3$ formation (Fig. 7c) are determined solely by O_2 dissociation, carbon selectivities toward CO_2 and $HCOOCH_3$ vary with both CH_3OH and O_2 pressures. $HCOOCH_3$ formation requires dehydrogenation of CH_2O^* to CHO* followed by reaction of CHO* with a vicinal CH_3O^*, but CO_2 formation requires only the CH_2O^* dehydrogenation step without CH_3O^* involvement along its reaction path. The different molecularity arising from the CH_3O^* involvement for $HCOOCH_3$ formation and not for CO_2 formation lead the rate ratio of $HCOOCH_3$ to CO_2 formation to vary proportionally with $[CH_3O^*][*]^{-1}$ (data not shown here; $[CH_3O^*]$ denotes the concentration of adsorbed CH_3O^* on platinum surface sites), as derived in Appendix, Section A.3.

3.6. Methanol partial oxidation on Pt cluster surfaces saturated with CH_3OH derived species (Regime 1)

As O_2-to-CH_3OH ratio decreases further to less than 0.5, rate dependencies for HCHO, $HCOOCH_3$, and CO_2 formation from CH_3OH–O_2 reactions on Pt clusters (3.0 nm mean Pt cluster diameter, 373 K) undergo another transition. The effective reaction orders with respect to O_2 are nearly or equal to two for all species ($\beta_{HCHO,1} = \beta_{CO_2,1} = 1.7 \pm 0.2$, $\beta_{HCOOCH_3,1} = 2 \pm 0.2$) and with respect to CH_3OH are nearly negative one for HCHO and CO_2 formation ($\alpha_{HCHO,1} = \alpha_{CO_2,1} = -0.7 \pm 0.2$) and zero order for $HCOOCH_3$ formation ($\alpha_{HCOOCH_3,1} = 0 \pm 0.1$), as summarized in Table 3. The rates of HCHO formation and combined rates of CO_2 and $HCOOCH_3$ formation are plotted in terms of $r_{j,1}[CH_3OH]^{-1}$ (subscript j denotes either HCHO or lump of secondary products CO_2 and $HCOOCH_3$, ($CO_2 + HCOOCH_3$), and subscript 1 denotes Regime 1) vs. the O_2-to-CH_3OH ratio (0.1–2.5 kPa O_2 and 2.5–4.5 kPa CH_3OH) in Fig. 8a and b, respectively.

These rate dependencies are consistent with CH_3OH activation on Pt surfaces predominantly covered by CH_3OH derived intermediates, likely CH_3O^*, as the kinetically-relevant step. On cluster surfaces scarce of unoccupied Pt sites, adsorbed diatomic oxygen (O_2^*) may assist with CH_3O^* decomposition. Mechanistic involvement of O_2^* was proposed in CH_3OH activation on Pt(1 1 1) surfaces without further kinetic analysis at 35–100 K [29] and 100–550 K [28,36]. The involvement of diatomic oxygen leads the fraction of CH_3O^*-to-$*$ on Pt clusters, $[CH_3O^*]\,[*]^{-1}$, to vary proportionally to CH_3OH-to-O_2 ratio. These assumptions lead to an expression for $r_{ODH,1}[CH_3OH]^{-1}$ as a function of O_2-to-CH_3OH ratio according to (derivation in Appendix Section A.5):

$$\frac{r_{ODH,1}}{[CH_3OH]} = \frac{k_{1.3}[CH_3OH^*][*]}{[CH_3OH]([*]+[CH_3O^*])^2} = \frac{k_{1.3}K_{1.2}}{\left(1+\frac{k_{1.3}K_{1.2}[CH_3OH]}{k_{1.4}K_{1.1}[O_2]}\right)^2} \tag{9}$$

where $K_{1.1}$ and $K_{1.2}$ reflect the equilibrium constants for O_2 (Step 1.1, Scheme 2) and CH_3OH (Step 1.2, Scheme 2) adsorption on a Pt site, respectively; $k_{1.3}$ and $k_{1.4}$ are the rate constants for CH_3OH^* dissociation assisted by a vicinal Pt site (Step 1.3, Scheme 2) and for CH_3O^* reaction with vicinal O_2^* species (Step 1.4, Scheme 2), respectively. The involvement of oxygen (O_2^* or O*) in the initial CH_3OH activation is ruled out in this regime, because oxygen involvement would lead the rate of CH_3OH oxidative dehydrogenation, $r_{ODH,1}$, to acquire a first-order dependence with respect to O_2. The apparent reaction order with O_2 larger than one but below two ($\beta_{ODH,1} = \beta_{HCHO,1} = 1.7 \pm 0.2$) indicates that both the denominator terms, $k_{1.3}K_{1.2}[CH_3OH](k_{1.4}K_{1.1}[O_2])^{-1}$ and 1, in Eq. (9) are of comparable magnitudes. The ratio of these terms

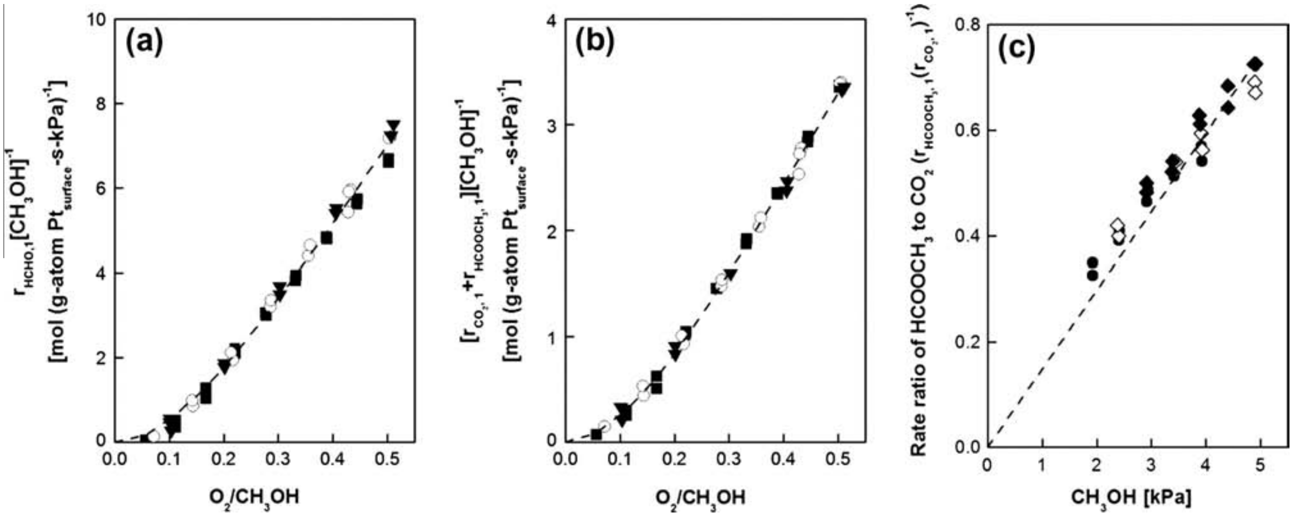

Fig. 8. (a) First-order rate coefficients ($r_{HCHO,1}[CH_3OH]^{-1}$) for HCHO formation and (b) first-order rate coefficients for the total rates of $HCOOCH_3$ and CO_2 formation $\{(r_{CO_2,1} + r_{HCOOCH_3,1})[CH_3OH^{-1}\}$ during CH_3OH–O_2 reactions with 2.5 kPa (▼), 3.5 kPa (○), and 4.5 kPa (■) CH_3OH on 1.0 wt% Pt/SiO_2 (3.0 nm mean Pt cluster diameter) as a function of O_2-to-CH_3OH ratio. (c) Rate ratio of $HCOOCH_3$ to CO_2, $r_{HCOOCH_3,1}$ $(r_{CO_2,1})^{-1}$, as a function of CH_3OH pressure during CH_3OH–O_2 reactions with 1.00 kPa (●), 1.25 kPa (◇), and 1.75 kPa (♦) of O_2 on 1.0 wt% Pt/SiO_2 (373 K, 4.2 × 10^7 cm^3 (g_{cat} h)$^{-1}$, 200 SiO_2-to-catalyst intra-particle and 5700 SiO_2-to-catalyst inter-particle dilution ratios).

{$k_{1.3}K_{1.2}[CH_3OH](k_{1.4}K_{1.1}[O_2])^{-1}/(1)$} reflects the fraction of CH_3O^*-to-$*$ during steady-state reactions. Non-linear regression of the rate data in Fig. 8a against Eq. (A.14) $r_{HCHO,1} = k_{1.5}(k_{1.5}+k_{1.6})^{-1}r_{ODH,1}$, where $k_{1.5}(k_{1.5}+k_{1.6})^{-1}$ denotes the selectivity for HCHO formation in the oxidative dehydrogenation step and $k_{1.5}$ and $k_{1.6}$ are the rate constants for desorption of HCHO and sequential hydrogen abstraction of $CH_2O_2^*$, respectively, see Appendix Section A.5} provides the ratios of these terms, presented in Fig. 9 as the fraction of unoccupied Pt sites, which increases from 0.01 to 0.33 as the O_2-to-CH_3OH ratio increases from 0.01 to 0.5 during steady-state CH_3OH catalysis in this regime.

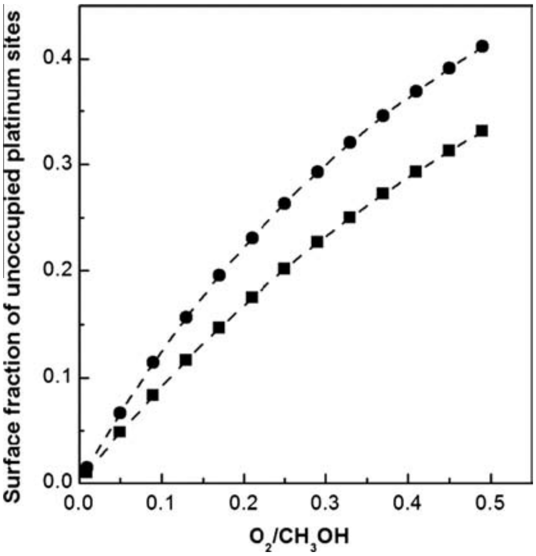

Fig. 9. Surface fraction of unoccupied platinum sites derived from non-linear regression fittings of rate data during CH_3OH–O_2 reactions on 1.0 wt% Pt/SiO_2 with 3.0 nm (■) and 4.8 nm (●) mean Pt cluster diameters in Regime 1 (0.01–0.50 O_2-to-CH_3OH ratio) with rate expression in Eq. (A.14) as a function of O_2-to-CH_3OH ratio (373 K, 4.2×10^7 cm^3 $(g_{cat}\ h)^{-1}$, 200 SiO_2-to-catalyst intra-particle and 5700 SiO_2-to-catalyst inter-particle dilution ratios).

Carbon selectivities are independent of O_2 pressure over the entire range of O_2-to-CH_3OH ratios in this regime, despite the variation in CH_3O^* and $*$ (Fig. 9) surface fractions, because both O_2^* and O^* are involved only for the formation of $CH_2O_2^*$ intermediates and not involved in any of the sequential reactions of $CH_2O_2^*$ that form HCHO, $HCOOCH_3$, and CO_2. These results indicate that all products are formed from surface intermediates directly derived from CH_3OH, consistent with the lack of residence time effects on selectivities in this regime (Fig. 3a, Section 3.2). The rate ratio for $HCOOCH_3$ to CO_2, however, increases linearly with increasing CH_3OH pressure, as shown in Fig. 8c, because $HCOOCH_3$ formation requires the recombination of two CH_3OH derived species, a step that becomes more favorable as CH_3OH pressure and coverages of CH_3OH derived intermediates increase.

3.7. Catalytic effects of mean cluster diameter and average Pt surface coordination during methanol partial oxidation on Pt cluster surfaces saturated with O^*, uncovered of reactive intermediates, and partially covered with CH_3OH derived intermediates

Next, we interrogate the catalytic effects of Pt surface coordination and thus the coverages and binding strengths of the various reactive intermediates (O^*, CH_3O^*) by varying the mean Pt cluster diameters from 3.0 nm to 4.8 nm. Pt atoms on small Pt cluster surfaces bind reactive intermediates much more strongly than those on large clusters because of their higher extent of coordinative unsaturation. These effects of surface coordination affect the coverages and binding strengths of the reactive intermediates and, in turn, alter both the rate and thermodynamic constants and the resulting rates and carbon selectivities. Figs. 10 and A.6 compare the HCHO formation and ODH rates (at 373 K), per exposed Pt atom, between two 1.0 wt% Pt/SiO_2 samples with different mean Pt cluster diameters of 3.0 nm and 4.8 nm and Table 4 summarizes the associated effective rate constants for HCHO formation for all regimes. The rates on both samples showed similar rate dependencies, but their values were higher for the larger than the smaller clusters.

These reactivity trends are interpreted next by correlating the changes in binding strengths and coverages to the rate and thermodynamic parameters that govern the catalytic rates in each regime. On O^* saturated surfaces (Regime 3), an increase in Pt

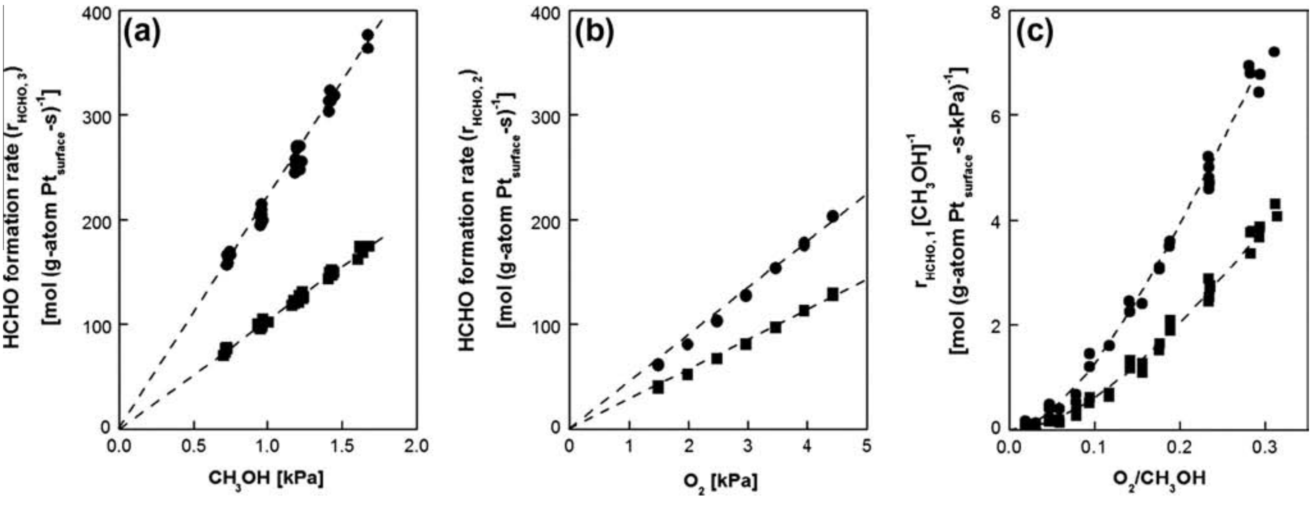

Fig. 10. (a) Rates of HCHO formation ($r_{HCHO,3}$) during CH_3OH–O_2 reactions on supported Pt clusters of different diameters {4.8 nm (●) and 3.0 nm (■)} in Regime 3 plotted as a function of CH_3OH pressure; (b) rates of HCHO formation ($r_{HCHO,2}$) during CH_3OH–O_2 reactions on supported Pt cluster of different diameters {4.8 nm (●) and 3.0 nm (■)} in Regime 2 plotted as a function of O_2 pressure; (c) first-order rate coefficients for HCHO formation ($r_{HCHO,1}$ $[CH_3OH]^{-1}$) on supported Pt cluster of different diameters {4.8 nm (●) and 3.0 nm (■)} in Regime 1 as a function of O_2-to-CH_3OH ratio. (373 K, 2.52×10^8 cm^3 $(g_{cat}\ h)^{-1}$, 1.26×10^8 cm^3 $(g_{cat}\ h)^{-1}$, and 4.2×10^7 cm^3 $(g_{cat}\ h)^{-1}$ for Regimes 3, 2, and 1, respectively, 200 SiO_2-to-catalyst intra-particle and 5700 SiO_2-to-catalyst inter-particle dilution ratios).

Table 4
Effects of mean Pt cluster diameter on effective rate constants for HCHO formation ($k^*_{eff,HCHO,i}$) during $CH_3OH–O_2$ reactions on 1.0 wt% Pt/SiO_2 at 373 K.

Mean Pt cluster diameter	Kinetic regimes and effective rate constants [mol (g atom $Pt_{surface}$ s kPa)$^{-1}$]		
	Regime 3^a ($k_{eff,HCHO,3}$)	Regime 2^b ($k_{eff,HCHO,2}$)	Regime 1^c ($k_{eff,HCHO,1}$)
O_2/CH_3OH ratio	10–45	0.5–10	0.01–0.5
3.0 nm	105 ± 5	28.4 ± 1.5	20.8 ± 0.6
4.8 nm	215 ± 5	44.8 ± 5.0	29.0 ± 1.0

(*: $k_{eff,HCHO,i}$, from linear regression of rate data in Figs. 10a and 10b with Eqs. (6) and (A.8) for Regimes 3 and 2, respectively, and from non-linear regression of rate data in Fig. 10c with Eq. (3) for Regime 1. ^{a}2.52 × 10^8 cm^3 $(g_{cat}\ h)^{-1}$, ^{b}1.26 × 10^8 cm^3 $(g_{cat}\ h)^{-1}$, ^{c}4.2 × 10^7 cm^3 $(g_{cat}\ h)^{-1}$; ^{a,b,c}: 200 SiO_2-to-catalyst intra-particle and 5700 SiO_2-to-catalyst inter-particle dilution ratios).

surface coordination with increasing cluster diameter leads to a concomitant decrease in the average binding strength of O* atoms. Density functional theory calculations predict a decrease in oxygen binding strength with increasing Pt coordination: from 133 to 96 kJ mol^{-1} as the Pt coordination number increases from 6.5 to 9.0 on the various surface sites on Pt clusters (201 Pt atoms in cubo-octahedral structures) at low O* coverages (0.01 ML) [40] and from 140 to 105 kJ mol^{-1} as the Pt coordination number increases from 7 to 9 on fcc-like surfaces on Pt(3 2 1) surfaces [57]. At the higher O* coverages, the trend between the oxygen binding strengths and Pt coordination numbers is expected to remain the same, even though oxygen binding strengths are weaken by the lateral repulsive interactions between the O* atoms [58]. The weakly bound O* prevalent on the larger clusters are more basic and thus more effective in electron donation to the leaving H during the O–H bond activation in CH_3OH, as reflected from an increase in the effective rate constant for HCHO formation ($k_{eff,HCHO,3}$) by a factor of 2.05 ± 0.10 for the larger than the smaller Pt clusters (Table 4). Similar effects of oxygen binding strength on their reactivity toward hydrogen abstraction were reported for alkane (CH_4 [39,40], C_2H_6 [41]) oxidation on Pt clusters.

The rates for oxidative dehydrogenation and HCHO formation on bare Pt clusters (Regime 2) vary less sensitively with cluster diameters and the coordinative unsaturation of Pt sites (Figs. A.6b and 10b). The effective rate constant for HCHO formation, $k_{eff,HCHO,2}$, increased by a factor of 1.57 ± 0.25 as cluster diameter increased from 3.0 to 4.8 nm (Table 4). These weak effects are expected because kinetically-relevant O_2 dissociation occurs on Pt sites via a late transition state with low activation barriers {20 kJ (mol O_2)$^{-1}$ on 1.8 nm cubo-octahedral Pt clusters (DFT calculated value) [39] and 8 kJ (mol O_2)$^{-1}$ on 3.3 nm Pt clusters (experimental value) [55]} that do not vary strongly with O* binding energy. We surmise that a small amount of CO* or CH_3O^* intermediates derived from CH_3OH may preferentially bind to coordinatively unsaturated corner and edge sites (as discussed in Section 3.5) at a higher surface fraction on the smaller than larger clusters. The fraction of site occupied by CO* or CH_3O^*, however, does not vary with reactant and product pressures because of their strong bindings to these sites (e.g., CO* adsorption energies on a Pt cluster are -171 kJ mol^{-1} on corner sites and -161 kJ mol^{-1} on edge sites, more negative than on terrace sites of -120 kJ mol^{-1} [56]) and therefore appear to be kinetically invisible. We surmise that the different fractions of site occupation by these intermediates between the larger and smaller clusters may lead to the higher rates and apparent weak structure sensitivity effects in this regime (Fig. 10b).

Turnover rates for ODH and HCHO formation remained larger for the larger than smaller clusters during CH_3OH oxidation on cluster surfaces predominantly covered with CH_3OH derived intermediates (Figs. A.6c and 10c). Non-linear regression fittings of the HCHO formation rates in this regime (Fig. 10c) to the rate equation {Eq. (A.14), $r_{HCHO,1} = k_{1.5}(k_{1.5} + k_{1.6})^{-1} r_{ODH,1}$, Section A.5 in Appendix} suggest that the surface fraction of unoccupied Pt sites is higher for the larger than smaller clusters (0.02–0.32 for 4.8 nm vs. 0.01–0.25 for 3.0 nm, O_2-to-CH_3OH = 0.01–0.33 at 373 K, Fig. 9), because of their weak bindings to reactive intermediates. Non-linear regression fittings give the $k_{1.4}K_{1.1}$ value of 1.58 ± 0.28 times higher and $k_{1.3}K_{1.2}$ a smaller value of 1.12 ± 0.12 times higher for the larger than smaller clusters (Table A.3), apparently because binding strengths affect the step of H abstraction of CH_3O^* by O_2^* more sensitively than that of CH_3OH activation on Pt sites. These effects of binding strength lead the ratio of $k_{1.3}K_{1.2}(k_{1.4}K_{1.1})^{-1}$ to decrease and the fractional coverage of unoccupied Pt sites and rates to concomitantly increase with increasing Pt cluster diameter.

The transition in surface coverages of Pt from saturated with oxidant derived species (Regime 3) to reductant derived species (Regime 1) in response to changing oxidant-to-reductant ratio alters the kinetically-relevant step from limited by reductant activation on O* site pairs (Regime 3) to oxidant activation on $*$ site pairs (Regime 2) and then to reductant activation on $*$ site pairs (Regime 1). These kinetic phenomena governed by changing chemical potentials at Pt cluster surfaces, as shown here using $CH_3OH–O_2$ reactions, appear to be general for oxidation reactions and have also been recognized and rigorously demonstrated recently for CH_4 [39,40], C_2H_6 [41], and CO oxidation [55,56].

4. Conclusion

Kinetic studies of $CH_3OH–O_2$ reactions over dispersed Pt clusters on SiO_2 show distinct rate dependencies that vary strictly with the O_2-to-CH_3OH ratios, because these ratios determine the oxygen and carbon chemical potential, identity and coverages of the reactive intermediates at Pt cluster surfaces and, in turn, the nature of active site structures and rates. The kinetically-relevant step undergoes transition from limited by CH_3OH activation on O* saturated Pt cluster surfaces to limited by O_2 dissociation on uncovered surfaces and then to CH_3OH activation on surfaces predominantly covered with CH_3OH derived intermediates. As a result of the transition, the reaction order with respect to O_2 increases whereas that with respect to CH_3OH concomitantly decreases as the O_2-to-CH_3OH ratios and oxygen chemical potential at Pt surfaces decrease. Chemisorbed oxygen atoms are reactive in CH_3OH activation steps, apparently by assisting with the hydrogen abstraction step, leading to larger CH_3OH conversion rates at the higher O_2-to-CH_3OH ratios. The Pt cluster diameter and the related average surface coordination influence the coverages and binding strengths of the reactive intermediates and, in turn, rates and selectivities. Larger Pt clusters contain coordinatively more saturated surface Pt sites than smaller Pt clusters and their weaker bindings to O* and CH_3OH derived intermediates have rendered them more reactive than the smaller Pt clusters. The identity of the kinetically-relevant step for oxidation reactions varies with the nature and surface coverages of the reactive intermediates, through which CH_3OH and O_2 dissociates and activates via different pathways mediated by either O* or $*$, and as a result, acquiring diverse rate dependencies that are demonstrated here to correlate strictly with the O_2-to-CH_3OH, which together with the rate constants for CH_3OH and O_2 activation steps, is a descriptor for the oxygen chemical potential at Pt cluster surfaces.

Acknowledgments

This study was supported by Natural Sciences and Engineering Research Council of Canada and Canada Foundation for Innovation. We also acknowledge Chinese Fundamental Research Funds for the Central Universities (No. CDJXS11142231) and China Scholarship Council for a fellowship awarded to Weifeng Tu. We thank Petar Lachkov for carrying out the experiments for H_2 and CO quantification and oxygen uptake measurements.

Appendix A. Supplementary material

Supplementary data associated with this article can be found, in the online version, at http://dx.doi.org/10.1016/j.jcat.2014.01.018.

References

[1] J. Lichtenberger, D. Lee, E. Iglesia, Phys. Chem. Chem. Phys. 9 (2007) 4902–4906.
[2] R. McCabe, P. Mitchell, Appl. Catal. 27 (1986) 83–98.
[3] R. McCabe, D. McCready, J. Phys. Chem. 90 (1986) 1428–1435.
[4] A. Wittstock, V. Zielasek, J. Biener, C. Friend, M. Bäumer, Science 327 (2010) 319–322.
[5] C. Bazilio, W. Thomas, U. Ullah, K. Hayes, Proc. R. Soc. Lond. A 399 (1985) 181–194.
[6] R. Ubago-Pérez, F. Carrasco-Marín, C. Moreno-Castilla, Catal. Today 123 (2007) 158–163.
[7] F.-W. Chang, H.-Y. Yu, L. Selva Roselin, H.-C. Yang, Appl. Catal. A-Gen. 290 (2005) 138–147.
[8] A.P.V. Soares, M.F. Portela, A. Kiennemann, Catal. Rev. 47 (2005) 125–174.
[9] P. Forzatti, E. Tronconi, A.S. Elmi, Appl. Catal. A-Gen. 157 (1997) 387–408.
[10] H. Zhao, S. Bennici, J. Shen, A. Auroux, J. Mol. Catal. A-Chem. 309 (2009) 28–34.
[11] Y. Fu, J. Shen, Chem. Commun. (2007) 2172–2174.
[12] H. Liu, E. Iglesia, J. Phys. Chem. B 109 (2005) 2155–2163.
[13] T.J. Yang, J.H. Lunsford, J. Catal. 103 (1987) 55–64.
[14] M. Ai, J. Catal. 77 (1982) 279–288.
[15] A.P.V. Soares, M. Farinha Portela, A. Kiennemann, L. Hilaire, J. Millet, Appl. Catal. A-Gen. 206 (2001) 221–229.
[16] W. Holstein, C. Machiels, J. Catal. 162 (1996) 118–124.
[17] P. Mars, D.W. Van Krevelen, Chem. Eng. Sci. 3 (1954) 41–59.
[18] A. Goodrow, A.T. Bell, J. Phys. Chem. C 111 (2007) 14753–14761.
[19] A.S. Elmi, E. Tronconi, C. Cristiani, J.P. Gomez Martin, P. Forzatti, G. Busca, Ind. Eng. Chem. Res. 28 (1989) 387–393.
[20] J. Liu, E. Zhan, W. Cai, J. Li, W. Shen, Catal. Lett. 120 (2008) 274–280.
[21] J. Greeley, M. Mavrikakis, J. Am. Chem. Soc. 124 (2002) 7193–7201.
[22] T. Watanabe, M. Ehara, K. Kuramoto, H. Nakatsuji, Surf. Sci. 603 (2009) 641–646.
[23] S. Akhter, J.M. White, Surf. Sci. 167 (1986) 101–126.
[24] S.R. Bare, J.A. Stroscio, W. Ho, Surf. Sci. 155 (1985) L281–L291.
[25] S. Sakong, A. Gross, J. Phys. Chem. A 111 (2007) 8814–8822.
[26] P. Chantaravitoon, S. Chavadej, J. Schwank, Chem. Eng. J. 97 (2004) 161–171.
[27] N. Pernicone, F. Lazzerin, G. Liberti, G. Lanzavecchia, J. Catal. 14 (1969) 293–302.
[28] M. Endo, T. Matsumoto, J. Kubota, K. Domen, C. Hirose, Surf. Sci. 441 (1999) L931–L937.
[29] T. Sawada, Z. Liu, N. Takagi, K. Watanabe, Y. Matsumoto, Chem. Phys. Lett. 392 (2004) 334–339.
[30] P. Gazdzicki, S. Thussing, P. Jakob, J. Phys. Chem. C 115 (2011) 23013–23022.
[31] C.J. Machiels, W.H. Cheng, U. Chowdhry, W.E. Farneth, F. Hong, E.M. Mc Carron, A.W. Sleight, Appl. Catal. 25 (1986) 249–256.
[32] J.N. Allison, W.A. Goddard, J. Catal. 92 (1985) 127–135.
[33] J. Gong, D.W. Flaherty, R.A. Ojifinni, J.M. White, C.B. Mullins, J. Phys. Chem. C 112 (2008) 5501–5509.
[34] I.E. Wachs, R.J. Madix, Surf. Sci. 76 (1978) 531–558.
[35] J.L. Davis, M.A. Barteau, Surf. Sci. 197 (1988) 123–152.
[36] M. Endo, T. Matsumoto, J. Kubota, K. Domen, C. Hirose, J. Phys. Chem. B 104 (2000) 4916–4922.
[37] D.A. Outka, R.J. Madix, J. Am. Chem. Soc. 109 (1987) 1708–1714.
[38] I.E. Wachs, R.J. Madix, J. Catal. 53 (1978) 208–227.
[39] Y.-H. Chin, C. Buda, M. Neurock, E. Iglesia, J. Am. Chem. Soc. 133 (2011) 15958–15978.
[40] Y.H. Chin, C. Buda, M. Neurock, E. Iglesia, J. Catal. 283 (2011) 10.
[41] M. García-Diéguez, Y.-H. Chin, E. Iglesia, J. Catal. 285 (2012) 260–272.
[42] D.R. Lide, Handbook of Chemistry and Physics, 87th ed., CRC Press, Boca Raton, FL, 2006.
[43] G. Martra, F. Arena, S. Coluccia, F. Frusteri, A. Mezzapica, A. Parmaliana, Stud. Surf. Sci. Catal. 130 (2000) 3591–3596.
[44] A. Ishikawa, M. Neurock, E. Iglesia, J. Am. Chem. Soc. 129 (2007) 13201–13212.
[45] B.M. Weiss, E. Iglesia, J. Phys. Chem. C 113 (2009) 13331–13340.
[46] S. Li, X. Lu, W. Guo, H. Zhu, M. Li, L. Zhao, Y. Li, H. Shan, J. Organomet. Chem. 704 (2012) 38–48.
[47] D.H. Ehlers, A. Spitzer, H. Lüth, Surf. Sci. 160 (1985) 57–69.
[48] P. Błoński, N. López, J. Phys. Chem. C 116 (2012) 15484–15492.
[49] W.T. Lee, F. Thomas, R.I. Masel, Surf. Sci. 418 (1998) 479–483.
[50] B.A. Sexton, Surf. Sci. 102 (1981) 271–281.
[51] B.A. Sexton, K.D. Rendulic, A.E. Huges, Surf. Sci. 121 (1982) 181–198.
[52] E.M. Karp, T.L. Silbaugh, M.C. Crowe, C.T. Campbell, J. Am. Chem. Soc. 134 (2012) 20388–20395.
[53] L. Diekhöner, D.A. Butler, A. Baurichter, A.C. Luntz, Surf. Sci. 409 (1998) 384–391.
[54] S. Sakong, A. Groß, J. Catal. 231 (2005) 420–429.
[55] M. García-Diéguez, E. Iglesia, J. Catal. 301 (2013) 198–209.
[56] A.D. Allian, K. Takanabe, K.L. Fujdala, X. Hao, T.J. Truex, J. Cai, C. Buda, M. Neurock, E. Iglesia, J. Am. Chem. Soc. 133 (2011) 4498–4517.
[57] J. Bray, W. Schneider, Langmuir 27 (2011) 8177–8186.
[58] R.A. van Santen, M. Neurock, Molecular Heterogeneous Catalysis, Wily, 2002.